nature communications

Article

https://doi.org/10.1038/s41467-025-58791-6

GABAergic neurons in central amygdala contribute to orchestrating anxiety-like behaviors and breathing patterns

Received: 10 March 2024

Accepted: 2 April 2025

Published online: 14 April 2025

Check for updates

Xiaoyi Wang[1], Shangyu Bi[1], Ziteng Yue[1], Xinxin Chen[1], Yuhang Liu[1], Tianjiao Deng[1], Liuqi Shao[1], Xinyi Jing[1], Cuidie Wang[1], Yakun Wang[2], Wei He[1], Hongxiao Yu[1], Luo Shi[1], Fang Yuan[1,3] ✉ & Sheng Wang[1,3,4] ✉

Anxiety is characterized by dysregulated respiratory reactivity to emotional stimuli. The central amygdala (CeA) is a pivotal structure involved in processing emotional alterations, but its involvement in orchestrating anxiety-like behaviors and specific breathing patterns remains largely unexplored. Our findings demonstrate that the acute restraint stress (ARS) induces anxiety-like behaviors in mice, marked by prolonged grooming time and faster respiratory frequency (RF). Conversely, silencing GABAergic CeA neurons reduces post-ARS anxiety-like behaviors, as well as the associated increases in grooming time and RF. In actively behaving mice, stimulation of GABAergic CeA neurons elicits anxiety-like behaviors, concurrently prolongs grooming time, accelerates RF through a CeA-thalamic paraventricular nucleus (PVT) circuit. In either behaviorally quiescent or anesthetized mice, stimulation of these neurons significantly increases RF but does not induce anxiety-like behaviors through the CeA-lateral parabrachial nucleus (LPBN) circuit. Collectively, GABAergic CeA neurons are instrumental in orchestrating anxiety-like behaviors and breathing patterns primarily through the CeA-PVT and CeA-LPBN circuits, respectively.

Breathing is a complex and finely tuned rhythmic movement that is integral to various behaviors and states, including blood gas regulation, the volitional control needed for speech and breath-holding, and the emotional regulation observed in laughing, crying, and sighing[1,2]. While extensive studies have focused on the chemical regulation of breathing[3–5], the impact of emotions and behaviors on respiratory control remains less understood. Accumulated evidence indicates that negative emotions like fear, anxiety, panic, and anger trigger an increase in human ventilation, often measured as elevated minute ventilation (MV)[6] and varying tidal volume (TV)[2,7]. Conversely, positive emotions can also affect breathing patterns, typically resulting in more variable respiratory frequency (RF) and decreased TV and inspiration time[8–10]. In psychiatry conditions such as anxiety disorders, breathing patterns become faster and more superficial[11,12], often accompanied by increased apneic episodes during sleep and more frequent sighs when awake[13,14]. Thus, emotional changes can differentially influence breathing patterns, potentially leading to dysfunctional respiration. Moreover, different behaviors, such as grooming, sniffing and moving, are tightly associated with specific breathing patterns[15]. Understanding the neural pathways that mediate these emotional and behavioral influences on breathing patterns is essential for developing treatments and preventive strategies. However, the current evidence in this area remains limited.

The amygdala, which receives respiratory inputs, exhibits rhythmic activity that correlates with inspiratory activity signaled by the phrenic nerve root[16], suggesting that the amygdala's spontaneous

[1]Department of Neurobiology, Hebei Medical University, Shijiazhuang, China. [2]Department of Sleep Medicine, Third Hospital of Hebei Medical University, Shijiazhuang, China. [3]Hebei Key Laboratory of Neurophysiology, Shijiazhuang, China. [4]The Key Laboratory of Neural and Vascular Biology, Ministry of Education, Shijiazhuang, China. ✉e-mail: yuanfang@hebmu.edu.cn; wangsheng@hebmu.edu.cn

oscillatory behavior is interconnected with respiratory functions. Over 90% of the neurons in the central amygdala (CeA) are GABAergic, and the CeA serves as the primary output center within the amygdala complex[17–20]. The CeA is known to be pivotal in processing fear, anxiety, and stress[17,21,22], and it is intricately connected with various brain regions, forming complex neural circuits that underlie emotional and behavioral responses. The CeA receives inputs from cortical areas, such as the medial prefrontal cortex and dorsal peduncular area, and the hippocampus, which provide contextual information and threat appraisal[23,24], as well as projections from basolateral amygdala, which integrates sensory information and fear-related stimuli[25–27]. The CeA also interacts with the paraventricular nucleus (PVN)[28,29], paraventricular thalamic nucleus (PVT)[30,31], and the bed nucleus of the stria terminalis (BNST)[32,33]. These interactions are fundamental for the adaptive response to stress and involved in the habituation and learning of emotional responses. This complex network of neural circuits underscores the importance of determining whether the CeA acts as an integrative hub for emotional reactions and corresponding respiratory patterns. Neural tracing studies have revealed that the CeA has direct connections with key respiratory centers, including the preBötzinger complex (preBötC), lateral parabrachial nucleus (LPBN) and nucleus tractus solitarius (NTS)[1,34,35]. Despite these anatomical insights, the neural circuits linking respiratory patterns with emotional states remain incompletely understood.

In the present study, we investigated the hypothesis that GABAergic neurons in the CeA (hereafter called CeA^{GABA}) play a crucial role in integrating anxiety-like behaviors with their associated breathing patterns. We evaluated whether acute restraint stress (ARS) induced anxiety-like behaviors and specific respiratory changes in mice. Furthermore, we examined whether activating CeA^{GABA} neurons elicited anxiety-like behaviors and modified respiratory patterns during both active states and periods of behavioral quiescence. Our findings suggest that CeA^{GABA} neurons hold a significant role in harmonizing anxiety-like behaviors with the associated breathing patterns.

Result

Respiratory and behavioral changes after ARS

To evaluate anxiety-like behaviors and the associated breathing patterns, we utilized ARS animals, a well-established and noninvasive stress model[36], by restraining the C57BL/6J mice in custom-made tubes for 30 min. The mice were divided into 3 groups: a home cage group, a new cage group (transferred from their home cages to new cages 30 min prior to behavioral testing), and an ARS group that underwent a 30-min ARS, followed by a series of time-point behavioral evaluations (Supplementary Fig. 1a). We employed open field test (OFT) and elevated plus maze (EPM) assessments at intervals of 0, 15, 30, 40, 50 and 60 min following a 30-min restraint, comparing the results with those of the home cage and new cage groups. Our observations revealed that mice subjected to ARS exhibited significantly reduced time spent in the center of the OFT arena, prolonged resting time and diminished overall travel distance (Supplementary Fig. 1b-f). Furthermore, these mice displayed fewer entries into, less time spent within, and shortened travel distances in the open arms of the EPM (Supplementary Fig. 1g–k). These behavioral differences were most pronounced at the 0, 15, 30, and 40-min post-ARS, but were not evident at 50 and 60 min when compared to the new cage group. Meanwhile, no marked differences were observed between home cage and new cage animals. Specifically, we examined the contribution of sex difference to the generation of ARS-induced anxiety-like behaviors using OFT and EPM tests. Analysis of behavioral tests indicated that ARS uniformly induced anxiety-like behaviors in both male and female mice (Supplementary Fig. 2). Consequently, we demonstrate that ARS induces anxiety-like behaviors in mice, which are particularly prominent during the immediate to 40-min period following stress exposure.

Next, we utilized whole body plethysmography (WBP) to analyze behavioral and respiratory changes in freely behaving mice over a 40-min period following restraint stress, a timeframe during which anxiety-like behaviors were evident based on the aforementioned behavioral tests. To control for environmental factors, the mice were transferred from their home cages into new cages (Fig. 1a). Given that mice exhibit different respiratory patterns in novel environments, each subject was acclimatized within the WBP chamber for 60 min prior to data collection. We depicted the RF over a 40-min period using distribution curves (Fig. 1b), which revealed a rightward shift in the distribution curve for ARS mice, accompanied by a prominent peak ranging from 5 to 6 Hz. This indicates a predominance of high-frequency respiratory episodes in mice subjected to ARS. We then sought to determine if there was a correlation between breathing patterns and ARS-induced anxiety-like behaviors. To this end, we evaluated the 40-min behavioral changes using WBP and concurrent video recordings, following established methodologies[15]. Based on specific breathing waveforms (Supplementary Fig. 3a-e) and video recordings (Supplementary Movie 1), we categorized the behaviors into active (including moving, groom, and sniff) and quiescent (including eupnea and sleep) states (Fig. 1c). As shown in Supplementary Fig. 3f, g, the fastest RF was observed during sniff, followed by moving, groom, eupnea and sleep. Groom, which is considered an indicator of anxiety-like behaviors, has an RF ranging from 3 to 10 Hz. Aggregate data indicated that, compared to control counterparts, ARS mice exhibited a significant increase in cumulative active time and a decrease in quiescent time (Fig. 1d). Specifically, the increased active time in ARS mice was primarily due to a substantial increase in grooming duration, a reduction in sniffing duration, and no significant change in moving duration. The reduced quiescence was marked by a significant decrease in sleep duration, while the time spent in eupnea was prolonged (Fig. 1e, f).

To analyze the time-series changes of the above behaviors, we disaggregated the data to examine the duration of each behavior in 5-min intervals over the 40-min period (Fig. 1g). Additionally, we conducted quantitative analyses to compare the cumulative time spent on each behavior in 5-min intervals between the new cage group and the ARS group over the 40-min period. These behaviors included moving (Fig. 1h), grooming (Fig. 1i), sniffing (Fig. 1j), eupnea (Fig. 1k), and sleeping (Fig. 1l). Meanwhile, ARS mice displayed a transient reduction in RF immediately after the ARS, followed by an elevation 20 to 30 min later compared to control mice (Fig. 1m). To elucidate the relationship between grooming and RF, correlation analyses were conducted based on data obtained from WBP recordings and OFT (Supplementary Fig. 4). Our results revealed a significant positive correlation between RF and grooming time, suggesting that increased RF is associated with heightened anxiety levels, as indicated by the increased grooming behavior. Collectively, our findings demonstrate that ARS mice exhibit anxiety-like behaviors and elevated RF, particularly within 20 to 30 min following ARS treatment. This elevation in RF is closely linked to increased grooming activity, further supporting the notion that RF can be a valuable marker for assessing anxiety-like states.

Inhibition of CeA^{GABA} neurons diminishes ARS-induced anxiety-like behaviors and respiratory changes

Previous studies have demonstrated the important role of CeA^{GABA} neurons in the regulation of anxiety and other negative emotions[26,37–39]. To investigate whether these neurons participate in the regulation of ARS-induced anxiety-like behaviors, we employed in vivo fiber photometry to measure the Ca^{2+} levels of CeA^{GABA} neurons, which reflect neuronal activation. This was achieved by delivering an AAV virus encoding the calcium indicator GCaMP6m (AAV9-EF1α-DIO-GCaMP6m) into the CeA of Vgat-Cre mice under restraint conditions, with a control group placed in new cages (Supplementary Fig. 5a–e).

https://doi.org/10.1038/s41467-025-58791-6

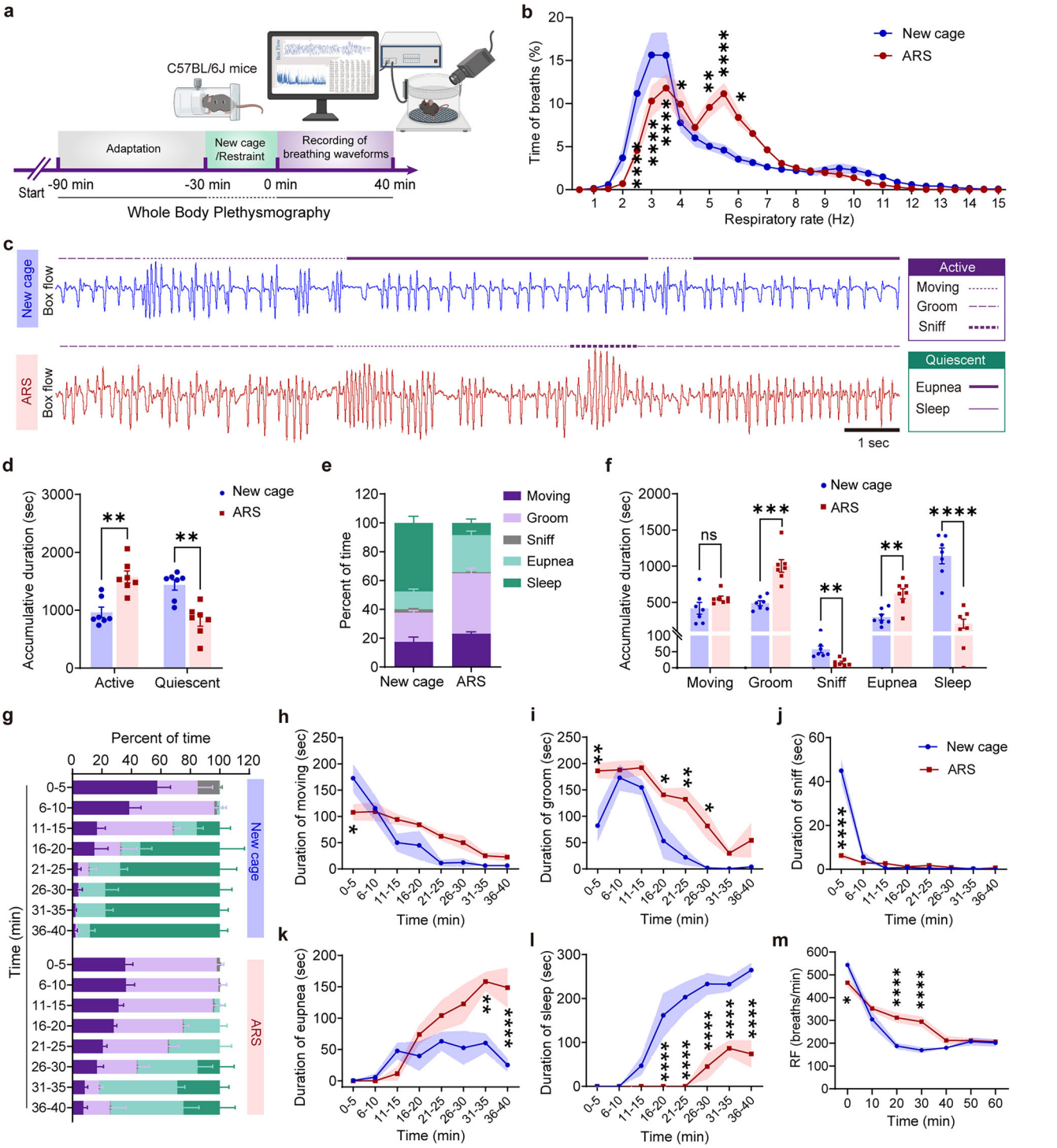

Fig. 1 | Respiratory and behavioral changes following acute restraint stress. **a** Schematic of the experimental procedure. **b** Distribution of RF (bin size 0.5 Hz) over a 40-min assay. $n = 10$ mice for both the new cage group and the ARS-treated group. $p = 0.0252$ for 4 Hz, $p = 0.0061$ for 5 Hz, $p = 0.0134$ for 6 Hz, $p < 0.0001$ for 2.5, 3, 3.5 and 5.5 Hz. **c** Example recordings of plethysmography airflow traces of the new cage group (blue) and ARS group (red). **d** Accumulative duration spent in active and quiescent states during 40-min plethysmography recording ($n = 7$ mice for each group). $p = 0.0023$ for active; $p = 0.0023$ for quiescent. Percent of time (**e**, $n = 7$ mice for each group) and accumulative duration (**f**, $n = 7$ mice for each group) of each behavior as defined in (**c**). After ARS, the duration of grooming and eupnea episodes increased, while the duration of sniff and sleep episodes decreased (groom, $p = 0.0006$; sniff, $p = 0.0065$; eupnea, $p = 0.0016$; sleep, $p < 0.0001$). **g** Percent of time spent on each behavior in every 5-min interval over 40 min ($n = 7$ mice for each group). Time-series change in the duration of moving (**h**), grooming (**i**), sniff (**j**), eupnea (**k**) and sleep (**l**) in every 5 min interval following new cage and ARS treatments. **h** 0–5 min, $p = 0.0206$. **i**, 0–5 min, $p = 0.0028$; 16–20 min, $p = 0.0186$; 21–25 min, $p = 0.0013$; 26–30 min, $p = 0.0439$. **j** 0–5 min, $p < 0.0001$. **k** 31–35 min, $p = 0.0017$; 36–40 min, $p < 0.0001$. **l** $p < 0.0001$ for 16–40 min. **m** A decrease in RF was observed immediately following the ARS, and elevated during 20 to 30 min ($n = 10$ mice per group). $p = 0.0271$ for 0 min, $p < 0.0001$ for 20 and 30 min. $^{*}p < 0.05$, $^{**}p < 0.01$, $^{***}p < 0.001$, $^{****}p < 0.0001$ by two-way ANOVA followed by Šídák's multiple comparisons test (**b**, **h**–**m**), two-tailed Mann–Whitney test (**d**, **f** moving), two-tailed unpaired *t* test followed by Welch's correction (**f**, groom and sniff) and two-tailed unpaired *t* test (**f**, eupnea and sleep). All data are presented as the mean ± SEM. ns, not significant. Source data is provided as a Source Data file. The materials depicted in (**a**) are created in BioRender. Xiaoyi, W. (2025) https://BioRender.com/i81e326. RF respiratory frequency, ARS acute restraint stress.

Upon introduction of the animals into new cages, a mild enhancement of Ca^{2+} signals was observed. In contrast, robust Ca^{2+} signals were detected in the 470 nm channel when mice were exposed to restraint stress, while the 410 nm channel showed minimal activity (Supplementary Fig. 5f). This notable increase in Ca^{2+} activity indicates that the activation level of CeA^{GABA} neurons was markedly elevated under restraint conditions compared to the new cage group (Supplementary Fig. 5g–i).

To further investigate whether CeA^{GABA} neurons regulate anxiety-like behaviors induced by ARS, a chemogenetic approach was employed to inhibit these neurons. We specifically expressed hM4Di (Designer Receptors Exclusively Activated by Designer Drugs, DREADDs) in CeA^{GABA} neurons by bilaterally delivering AAV-Ef1α-DIO-hM4Di-eYFP into the CeA of Vgat-Cre mice (Fig. 2a, b). Inhibition of hM4Di-expressing neurons was subsequently achieved through injections of clozapine-N-oxide (CNO, 2 mg/kg, i.p.). RNAscope fluorescence in situ hybridization (RNAscope-FISH) analysis confirmed the specificity and efficiency of hM4Di-eYFP expression in CeA^{GABA} neurons (Fig. 2c, d). Moreover, whole-cell patch clamp slice recordings revealed that bath application of CNO induced membrane hyperpolarization and a decrease in firing rate in CeA^{GABA} neurons (Fig. 2e), thereby confirming the inhibitory effect of hM4Di.

Next, we assessed the behavioral consequences of chemogenetic inhibition (Supplementary Fig. 6a) of CeA^{GABA} neurons using the OFT and EPM in both the new cage group (Supplementary Fig. 6b, left) and the ARS group (Supplementary Fig. 6b, right). The results showed that compared to saline injection, administration of CNO significantly increased the time spent in the center of the OFT and notably reduced resting time in the ARS group (Supplementary Fig. 6c–e). Similarly, CNO treatment increased both the number of entries into and the duration spent in the open arms of the EPM (Supplementary Fig. 6f–h). However, in non-stressed naïve mice, no significant differences in these behavioral assays were observed between saline and CNO treatments. Collectively, our findings indicated that the chemogenetic inhibition of CeA^{GABA} neurons significantly alleviated ARS-induced anxiety-like behaviors.

Next, we determined the impact of chemogenetic inhibition of CeA^{GABA} neurons on behavioral and respiratory changes following ARS. After a 60-min adaptation in the WBP chamber, mice were intraperitoneally injected with either saline or CNO, and then underwent a 30-min restraint, followed by a 40-min WBP recording (Fig. 2f). The distribution curves of RF over a 40-min period showed a leftward shift in the ARS group injected with CNO relative to those treated with saline, indicating a predominance of slow-frequency breathing pattern (3–3.5 Hz) (Fig. 2g). Furthermore, compared to saline treatment, CNO administration significantly reduced active time and increased quiescent time (Fig. 2h). This reduction in active time was specifically manifested as a decrease in stress-related grooming time and an increase in eupnea time, without affecting sniffing or sleeping activities (Fig. 2i, j). The behavioral data, analyzed in 5-min intervals, revealed that the inhibition of CeA^{GABA} neurons reduced stress-related grooming to varying degrees across each interval (Fig. 2k), with a particularly significant decrease observed at the 31 to 35-min mark (Fig. 2m). Additionally, compared to mice injected with saline, those receiving CNO exhibited a significant reduction in RF at the 20- and 30-min marks post-ARS (Fig. 2q). These results suggest that the reduction in stress-related grooming time is correlated with a decreased RF during the 31 to 35-min interval following ARS. For control experiments, neither saline nor CNO injections produced significant behavioral and respiratory changes in ARS-treated mice or their control counterparts, both of which received injections of a virus lacking the hM4Di gene into the CeA (Supplementary Fig. 7). Additionally, neither saline nor CNO injections had notable effects on breathing parameters in non-stressed naïve mice (Supplementary Fig. 8).

To further investigate whether inhibition of CeA^{GABA} neurons affects central respiratory drive, we concurrently utilized an optogenetic approach and phrenic nerve discharge (PND) recordings in bilaterally vagotomized, mechanically ventilated, anesthetized mice. This was achieved by delivering a virus encoding enhanced halorhodopsin (eNpHR) into the CeA of Vgat-Cre mice (Supplementary Fig. 9a). Four weeks after virus injections, immunohistochemical validation and RNAscope-FISH confirmed the specific expression of eNpHR in CeA^{GABA} neurons (Supplementary Fig. 9b–d). Whole-cell patch clamp slice recordings showed that illumination caused membrane hyperpolarization in CeA^{GABA} neurons, confirming the inhibitory effect generated by eNpHR activation (Supplementary Fig. 9e). Subsequently, illumination did not produce any notable changes in both the frequency and amplitude of PND in anesthetized mice (Supplementary Fig. 9f, g). Therefore, optogenetic inhibition of CeA^{GABA} neurons had no significant effect on central respiratory drive. Taken together, these data suggest that the inhibition of CeA^{GABA} neurons significantly alleviates ARS-induced anxiety-like behaviors, and reduces ARS-induced prolonged grooming time and high-frequency respiratory episodes.

Chemogenetic activation of CeA^{GABA} neurons induces anxiety-like behaviors and regulates behavior-related breathing patterns

To further examine whether the activation of CeA^{GABA} neurons affected behavioral patterns and the associated breathing patterns, we simultaneously conducted in vivo Ca^{2+} signal recordings in CeA^{GABA} neurons and WBP recordings following a 30-min restraint period (Supplementary Fig. 10a, b), as described above (Supplementary Fig. 5). This approach allowed us to concurrently monitor grooming-related respiratory waveforms and the dynamics of the Ca^{2+} signal (Supplementary Fig. 10c). Our results revealed that grooming-related respiratory waveforms were synchronized with enhanced Ca^{2+} signal of CeA^{GABA} neurons (Supplementary Fig. 10d, e). These findings suggest that grooming behavior is tightly associated with the heightened activation level of CeA^{GABA} neurons, highlighting the significant contribution of these neurons to regulating grooming.

Given that silencing CeA^{GABA} neurons significantly alleviated ARS-induced anxiety-like behaviors, we sought to test whether activation of these neurons could elicit anxiety-like behaviors. To this end, an optogenetic approach was employed by delivering a virus encoding ChR2 fused with mCherry (AAV9-Ef1α-DIO-ChR2-mCherry) into the CeA of Vgat-Cre mice. Control mice were injected with AAV9-Ef1α-DIO-eYFP, which lacks ChR2 gene (Supplementary Fig. 11a). OFT and EMP data showed that photostimulation notably induced anxiety-like behaviors (Supplementary Fig. 11b, c), underscoring the important contribution of CeA^{GABA} neurons to generation of anxiety-like behaviors.

Based on previous studies showing that the left and right CeA may differentially regulate anxiety-like behaviors[40,41], we hypothesized that photostimulation on different sides might have lateralized effects. To address this hypothesis, an optogenetic approach was employed to illuminate ChR2-expressing CeA^{GABA} neurons on the left and right CeA, respectively (Supplementary Fig. 12a–c). Data from the OFT and EPM revealed that photostimulation of CeA^{GABA} neurons, regardless of whether they were located on the left or right CeA, induced anxiety-like behaviors, with no significant lateralized effects observed (Supplementary Fig. 12d–i).

To elucidate the influence of CeA^{GABA} neuron activation on behavioral and breathing patterns, chemogenetic stimulation was undertaken in Vgat-Cre mice. These neurons were bilaterally transfected with AAV9-Ef1α-DIO-hM3Dq-mCherry, and the expression was visually detected through subsequent immunohistochemical staining (Fig. 3a, b). The cell-type specificity of hM3Dq-mCherry expression was confirmed using RNAscope-FISH (Fig. 3c, d). Moreover, the

https://doi.org/10.1038/s41467-025-58791-6

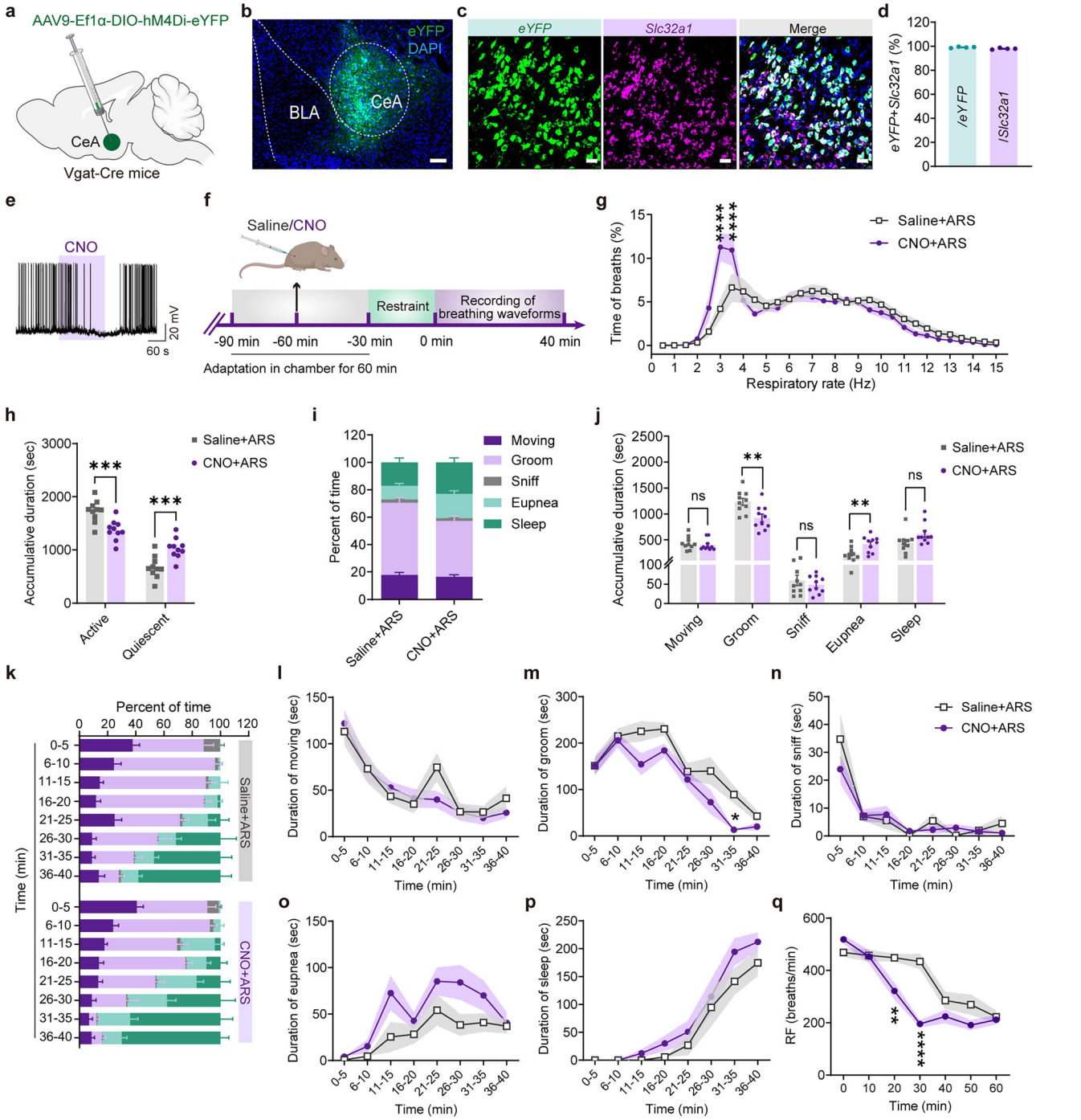

Fig. 2 | Silencing of CeA^{GABA} neurons reduces ARS-induced respiratory and behavioral changes. a Schematic of the chemogenetic strategy by delivering a virus encoding hM4Di into the CeA. **b** Representative image showing immunohistochemical detection of hM4Di expression (green) in the CeA. Scale bar, 100 μm. **c** RNAscope-FISH images demonstrating colocalization of hM4Di (green) and *Slc32a1* (Vgat, pink) mRNA. Scale bars, 20 μm. **d** Quantitative analysis confirming specific expression of hM4Di-eYFP in CeA^{GABA} neurons. $n = 4$ mice. **e** Representative traces showing that bath application of CNO (5 μM) induced membrane hyperpolarization in a hM4Di-expressing CeA^{GABA} neuron, as measured by whole-cell patch clamp slice recordings. **f** Schematic of the experimental procedure. **g** Distribution of RF (bin size 0.5 Hz) over a 40-min assay of ARS mice injected with saline and CNO. $n = 12$ mice per group. $p < 0.0001$ for 3 and 3.5 Hz. **h** Accumulative duration spent in active and quiescent states ($n = 10$ mice for each group). $p = 0.0008$ for active; $p = 0.0008$ for quiescent. Percent of time (**i**, $n = 10$ mice for each group) and accumulative duration (**j**, $n = 10$ mice for each group) of each behavior defined in Fig. 1c. CNO injection significantly reduced ARS-induced prolonged grooming time and increased eupnea duration (groom, $p = 0.0059$; eupnea, $p = 0.0078$). **k** Percent of time spent on each behavior in every 5-min interval ($n = 10$ mice for each group). Time-series changes in the duration of moving (**l**), grooming (**m**), sniff (**n**), eupnea (**o**) and sleep (**p**) in every 5 min. (**m**, 31-35 min, $p = 0.0395$). **q** CNO injection significantly decreased RF at 20- and 30-min mark post-ARS compared to saline treatment. $p = 0.0028$ for 20 min and <0.0001 for 30 min. $^{*}p < 0.05$, $^{**}p < 0.01$, $^{****}p < 0.0001$ by two-way ANOVA with Bonferroni's multiple comparisons tests (**g**, **l**–**q**) and two-tailed unpaired *t*-test (**h**, **j**). All data are presented as the mean ± SEM. Source data is provided as a Source Data file. The materials depicted in panels **a** and **f** are created in BioRender. Xiaoyi, W. (2025) https://BioRender.com/i81e326.

https://doi.org/10.1038/s41467-025-58791-6

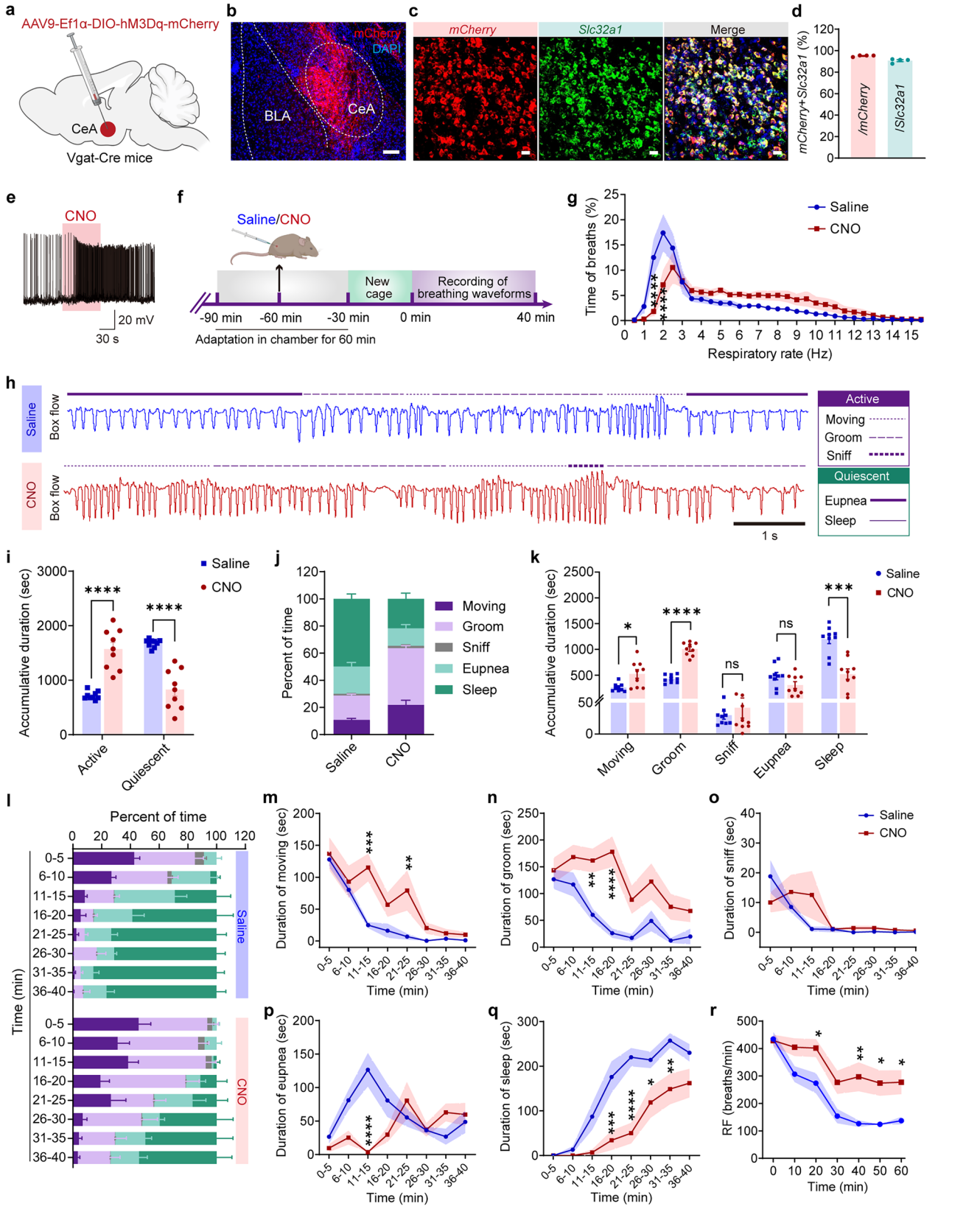

electrophysiological profile of hM3Dq was verified by demonstrating an increased firing rate upon bath application of CNO using whole-cell patch clamp slice recordings (Fig. 3e). Following a 60-min adaptation period, mice were administered either saline or CNO (1 mg/kg, i.p., Fig. 3f). WBP recordings demonstrated that, compared to saline injection, CNO administration significantly increased high-frequency respiratory episodes (Fig.3g, h). This respiratory change was accompanied by an increase in the duration of active behaviors (Fig. 3i), characterized by extended periods of moving and grooming. Meanwhile, there was a significant reduction in sleep time, which primarily resulted in decreased quiescent time (Fig. 3j, k). Furthermore, an analysis of 5-min intervals of each behavior over 40 min revealed that

Fig. 3 | Respiratory and behavioral changes following activation of CeA^{GABA} neurons. a Schematic diagram of the chemogenetic strategy by delivering a virus containing hM3Dq into the CeA from Vgat-Cre mice. **b** Representative image of immunohistochemical detection of hM3Dq expression in CeA neurons. Scale bar, 100 μm. **c** RNAscope-FISH images showing colocalization of hM3Dq (red) and *Slc32a1* (green) mRNA in CeA^{GABA} neurons. Scale bars, 20 μm. **d** Quantitative analysis of the efficiency and specificity of hM3Dq-mCherry. $n = 4$ mice. **e** Representative traces showing that bath application of CNO (5 μM) significantly increased firing in a hM3Dq-expressing CeA^{GABA} neuron, as measured by whole-cell patch clamp slice recordings. **f** Schematic of the experimental procedure. **g** Distribution of RF (bin size 0.5 Hz) over 40-min assay in saline and CNO injected groups ($n = 13$ mice per group). $p < 0.0001$ for 1.5 and 2 Hz. **h** Representative plethysmography airflow traces of saline and CNO treated groups. **i** Accumulative duration spent in active and quiescent states during 40-min plethysmography recordings ($n = 9$ mice per group). Active: $p < 0.0001$; Quiescent: $p < 0.0001$. Percent of time (**j**, $n = 9$ mice for each group) and accumulative duration (**k**, $n = 9$ mice for each group) of each behavior defined in (**h**). Compared to saline group, moving and grooming episodes increased, and sleeping time decreased. Moving, $p = 0.0149$; Groom, $p < 0.0001$; Sleep, $p = 0.0001$. **l** Percent of time spent on each behavior in every 5-min interval over 40 min ($n = 9$ mice for each group). Duration of moving (**m**), grooming (**n**), sniff (**o**), eupnea (**p**) and sleep (**q**) in every 5 min. $n = 9$ per group. **m**, 11–15 min, $p = 0.0004$; 21–25 min, $p = 0.0077$. **n**, 11–15 min, $p = 0.0058$; 16–20 min, $p < 0.0001$. **p**, 11–15 min, $p < 0.0001$. **q**, 16–20 min, $p = 0.0001$; 21–25 min, $p < 0.0001$; 26–30 min, $p = 0.0245$; 31–35 min, $p = 0.0064$. **r** CNO injection increased high-frequency respiratory episodes. $n = 13$ mice per group. 20 min, $p = 0.0436$; 40 min, $p = 0.0021$; 50 min, $p = 0.0100$; 60 min, $p = 0.0199$. $^{*}p < 0.05$, $^{**}p < 0.01$, $^{***}p < 0.001$, $^{****}p < 0.001$ by two-way ANOVA with Bonferroni's multiple comparisons tests (**g**, **m**–**r**), two-tailed unpaired *t*-test (**k**, groom, eupnea, sleep), two-tailed unpaired *t*- test with Welch's correction (**i**, **k**, moving, sniff). All data are presented as the mean ± SEM. Source data are provided as a Source Data file. The materials depicted in (**a**, **f**) are created in BioRender. Xiaoyi, W. (2025) https://BioRender.com/i81e326.

CNO injection, relative to saline treatment, significantly increased the duration of moving and grooming (Fig. 3l–n), while decreasing the duration of eupnea and sleep (Fig. 3p, q). Additionally, the RF was significantly higher during the 60-min period following CNO administration compared to saline treatment (Fig. 3r). Together, these findings provide reliable evidence that the activation of CeA^{GABA} neurons can induce anxiety-like behaviors and modulate behavior-specific breathing patterns, particularly by increasing active behaviors such as moving and grooming, and decreasing quiescent behaviors.

In addition to assessing above behavior-related breathing patterns, we also analyzed certain specific breathing patterns in mice following sufficient adaptation in the WBP chamber, including sigh and different types of apneas (Supplementary Fig. 13a–d). Previous studies have indicated that sigh[42] and sniff[43] are associated with anxiety-like behaviors in mice. However, our findings revealed no significant differences in these breathing patterns between saline and CNO injections (Supplementary Fig. 13e–i). Altogether, we suggest that the activation of CeA^{GABA} neurons induces anxiety-like behaviors in mice, characterized by prolonged time of grooming behavior and increased high-frequency respiratory episodes.

Photostimulation of CeA^{GABA} neurons activates breathing under both behaviorally quiescent and anesthesia conditions

While we demonstrate that the activation of CeA^{GABA} neurons elicited increased grooming behavior and concomitant high RF, it remains unexplored whether this stimulation triggers similar respiratory phenotypes under both behaviorally quiescent and anesthesia states. To address this question, we employed the aforementioned optogenetic approach by injecting AAV9-Ef1α-DIO-ChR2-mCherry (with AAV9-Ef1α-DIO-eYFP serving as a control virus) into the CeA of Vgat-Cre mice (Fig. 4a). The expression of ChR2 in the CeA was confirmed through immunohistochemical validation (Fig. 4b). Electrophysiological assays further confirmed that photostimulation of ChR2-expressing neurons in brain slices evoked action potentials (Fig. 4c). RNAscope-FISH analysis revealed the specific expression of ChR2-mCherry in GABAergic neurons within the CeA (Fig. 4d–e).

Subsequently, we examined the impact of CeA^{GABA} neuron photostimulation on ventilation using WBP recordings when the animals were behaviorally quiescent (Fig. 4f). Distribution curves of RF over 1 min revealed that photostimulation primarily increased the high-frequency respiratory episodes (Fig. 4g, h). Moreover, photostimulation at frequencies of ≥5 Hz significantly increased both RF and MV in mice expressing ChR2, compared to those expressing eYFP only, with no significant change in TV (Fig. 4i). In addition, we also assessed the lateralized effect of the CeA^{GABA} neuron photostimulation on ventilation and found no discrepancies between left and right CeA stimulations (Supplementary Fig. 14).

To further elucidate the influence of CeA^{GABA} neuron activation on the central respiratory drive, we examined the photostimulation effect on PND in bilaterally vagotomized, mechanically ventilated, ChR2-injected, anesthetized mice (Fig. 4j). Our observations demonstrated that the illumination over the CeA region produced a rapid, reversible, and moderate increase in PND frequency but did not affect the amplitude (Fig. 4k-m). Collectively, photostimulation of CeA^{GABA} neurons considerably enhances resting ventilation under both behaviorally quiescent and anesthesia conditions.

As previously reported[44] and illustrated in Allen Brain Atlas (http://www.brain-map.org), the CeA contains a high density of GABAergic neurons, with relatively sparse glutamatergic neurons that predominantly express Vglut1 rather than Vglut2. To examine whether the glutamatergic neurons in the CeA modulated anxiety-like behaviors and breathing patterns, we employed both chemogenetic and optogenetic approaches, as described above, to selectively stimulate these neurons. Chemogenetic stimulation of glutamatergic CeA neurons did not affect either behavioral or breathing patterns, as evidenced by WBP recordings (Supplementary Fig. 15a–h). Similarly, data from OFT and EPM showed that photostimulation produced no anxiety-like behaviors (Supplementary Fig. 15k–p), nor did it alter breathing parameters (Supplementary Fig. 15q–s). Therefore, the activation of glutamatergic CeA neurons has no discernible effect on anxiety-like behaviors or breathing patterns.

Effect of stimulation of downstream targets innervated by CeA^{GABA} neurons on respiratory phenotypes

Subsequently, we aimed to elucidate the circuit mechanisms underlying the aforementioned behavioral and respiratory effects. Initially, we utilized an AAV encoding modified wheat germ agglutinin (mWGA) gene (Supplementary Fig. 16a), a previously established method for anterograde transsynaptic tracing[45]. This approach enabled us to identify the fluorescent somata of postsynaptic neurons. Our neural tracing data revealed a diverse array of downstream targets innervated by CeA^{GABA} neurons (Supplementary Fig. 16b–y). Notably, these targets included brainstem areas relevant to respiration control, such as the NTS, preBötC, locus coeruleus (LC), and LPBN (Fig. 5a–g). To further corroborate these findings, we also applied a conventional anterograde tracing virus to map the efferent projections of CeA^{GABA} neurons (Supplementary Fig. 17a, b). The projection profile obtained using this method was consistent with those derived from mWGA tracing, confirming the connectivity between CeA^{GABA} neurons and the identified brainstem targets (Supplementary Fig. 17c–g).

Central respiratory drive is primarily generated by the respiratory central pattern generators and its modulatory inputs, with the preBötC being a core component of inspiratory rhythm generation in mammals[3–5]. Preinspiratory preBötC Dbx1^{+} neurons are rhythmogenic, while inspiratory preBötC Dbx1^{+} and somatostatin-expressing neurons

https://doi.org/10.1038/s41467-025-58791-6

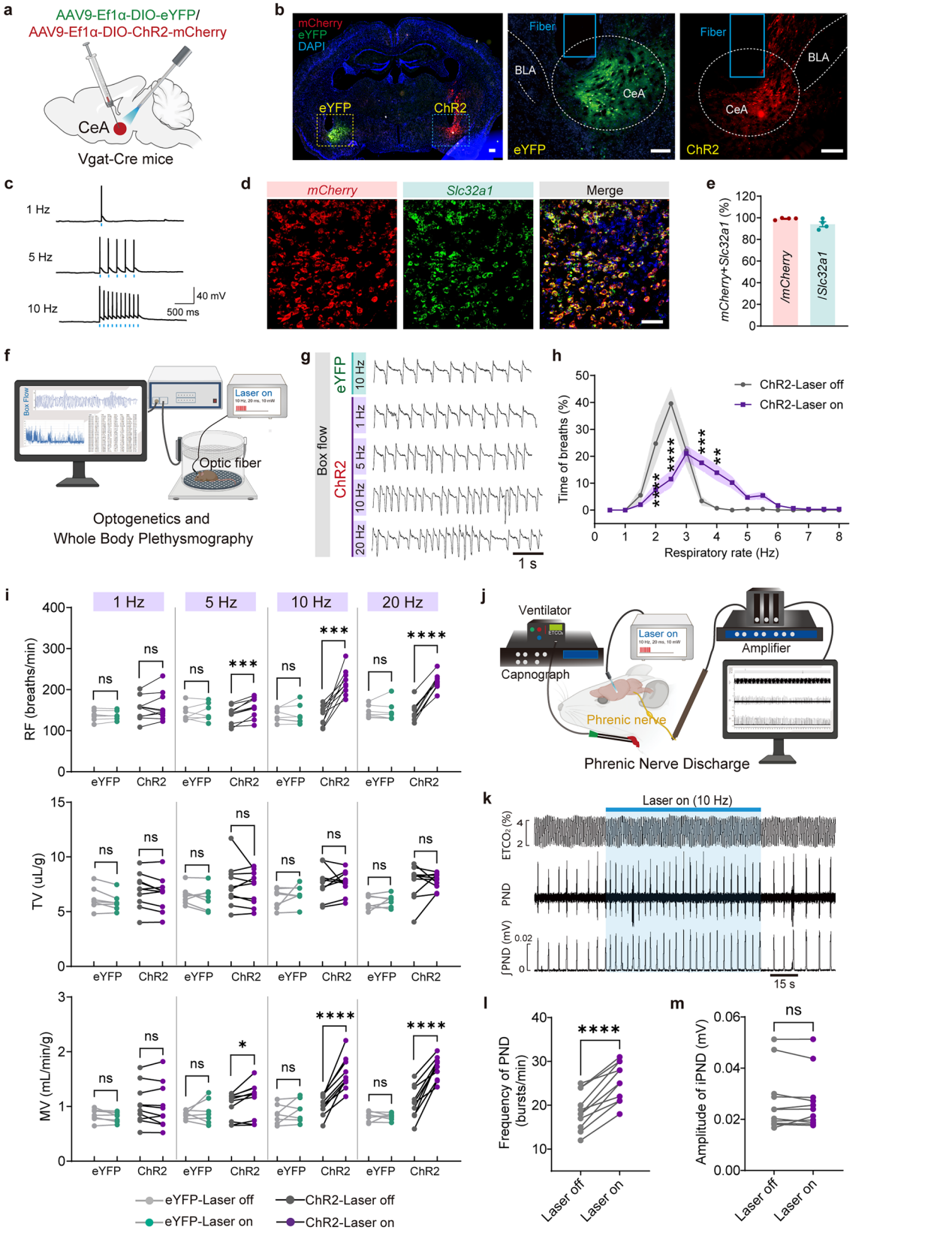

primarily act to shape motor output pattern[46]. Central respiratory chemoreceptors, located within the NTS, retrotrapezoid nucleus (RTN), and LC, provide excitatory drive to the preBötC[1,47,48]. The LPBN plays a critical role in regulating the phase transitions of breathing[5]. Moreover, a specific subset of *Tac1*-expressing neurons within the LPBN exerts potent and precise conditional control over breathing, capable of achieving physiological maximum through mechanisms that differ from the automatic control of breathing. This is important for the integration of breathing with state-dependent behaviors and emotions[49]. Taken together, these mapping insights indicate that CeA^{GABA} neurons may differentially influence respiratory motor output through their connections to these respiratory nuclei. To determine

Fig. 4 | Photostimulation of CeA^{GABA} neurons activates breathing under quiescence and anesthesia conditions. a Schematic of the optogenetic strategy involving the delivery of a virus encoding ChR2 or a control virus lacking ChR2 in Vgat-Cre mice. **b** Immunohistochemical validation of ChR2 expression. Left image: eYFP$^+$ (left, green) and ChR2-mCherry$^+$ (right, red) neurons in the CeA and tracks of fibers implantation. The middle and right confocal images are enlarged views of the regions denoted by the squares in the left image. Scale bars, 200 μm. **c** Whole-cell patch clamp slice recordings of light-evoked action potentials in a CeA^{GABA} neuron confirming the excitatory effect of ChR2 activation. **d** RNAscope-FISH images showing colocalization of ChR2 (red) and *Slc32a1* (green) mRNA. Scale bar, 50 μm. **e** Quantitative analysis of the efficiency and specificity of ChR2-mCherry expression. $n = 4$ mice. **f** Schematic diagram of optogenetics and WBP. **g** Typical respiratory waveforms showing the photostimulation effects on ventilation. **h** Distribution of RF (bin size 0.5 Hz) over a 1-min assay. $n = 10$ per group. $p < 0.0001$ for 2 and 2.5 Hz, $p = 0.0008$ for 3.5 Hz, $p = 0.0025$ for 4 Hz. **i** Quantitative analyses of the effects of illumination at different frequencies on breathing parameters. $n = 7$ for eYFP, $n = 10$ for ChR2. 5 Hz: $p = 0.0004$ for RF, $p = 0.0142$ for MV; 10 Hz: $p = 0.0001$ for RF, $p < 0.0001$ for MV; 20 Hz: $p < 0.0001$ for RF, $p < 0.0001$ for MV; ChR2-laser off *vs.* ChR2-laser on. **j** Schematic of PND recordings in bilaterally vagotomized, mechanically ventilated, anesthetized mice. **k** Representative traces showing that photostimulation of CeA^{GABA} neurons significantly increased PND activity. **l**, **m** Quantification of group data ($n = 11$ per group). **l,** $p < 0.0001$. $^*p < 0.05$, $^{**}p < 0.01$, $^{***}p < 0.001$, $^{****}p < 0.0001$ by two-way ANOVA followed by Šídák's multiple comparisons test (**h**), two-tailed paired *t*-test (**i**, **l**) and two-tailed Wilcoxon matched-pairs signed rank test (**m**). All data are presented as the mean ± SEM. Source data is provided as a Source Data file. The materials depicted in (**a**, **f**, **j**) are created in BioRender. Xiaoyi, W. (2025) https://BioRender.com/i81e326. PND phrenic nerve discharge.

the neural circuits potentially responsible for respiratory control by the CeA, we quantified the number of mWGA-labeled cells within the brainstem respiratory centers. Our analysis demonstrated a larger number of mWGA$^+$ neurons in the LPBN compared to those found in the NTS, preBötC, and LC (Fig. 5h). No mWGA$^+$ soma or fluorescent axon terminals were detectable in the RTN (Fig. 5h and Supplementary Fig. 17e).

We then proceeded with photostimulation of axon terminals in the LPBN, LC, NTS, preBötC, and RTN by expressing ChR2 in the CeA^{GABA} neurons of Vgat-Cre mice (Fig. 5i). Our results, depicted in Fig. 5j–s, revealed that photostimulation in these mentioned regions, with the exception of the RTN, significantly increased both RF and MV, but not TV in behaviorally quiescent mice. In line with these observations, photostimulation of axon terminals of CeA^{GABA} neurons projecting to the LPBN, LC, NTS and preBötC, respectively, increased the frequency but not the amplitude of PND in anesthetized mice (Supplementary Fig. 17i). Collectively, these findings suggest that CeA^{GABA} neurons regulate breathing through their projections to the brainstem respiratory centers.

The CeA-LPBN-preBötC circuit mediates excitatory drive to respiratory function

Given the pivotal role of the LPBN in modulating breathing patterns through its interaction with the preBötC[5], as well as the dense projections from CeA^{GABA} neurons to the LPBN, we sought to elucidate whether the CeA-LPBN-preBötC circuit considerably contributed to the regulation of aforementioned respiratory effects. To this end, we performed projection-specific manipulation experiments by delivering intersectional viral vectors to express hM3Dq in CeA^{GABA} neurons projecting to the LPBN (Fig. 6a). Immunohistochemical assays confirmed the presence of hM3Dq-mCherry in the CeA (Fig. 6b) and RNAscope-FISH verified the specific expression of hM3Dq in CeA^{GABA} neurons (Fig. 6c). Compared to saline injection, administration of CNO significantly increased the incidence of high-frequency respiratory episodes (Fig. 6d), with a marked elevation observed 30 min post-injection (Fig. 6e). Behavioral analyses revealed that both saline and CNO injections generated similar effects on active and quiescent periods, as well as the durations of moving, grooming, sniff, eupnea and sleep (Fig. 6f, g). These results suggest that the CeA-LPBN circuit primarily modulates breathing patterns without influencing behavioral alterations.

To address potential lateralized effects, we conducted a quantitative analysis of the density of axonal varicosities of CeA^{GABA} neurons projecting to the LPBN. Our results revealed a slightly denser distribution of these varicosities on the right side of the LPBN (Supplementary Fig. 18a–c). Moreover, photostimulation of CeA^{GABA} neuron axon terminals located on either the left or right LPBN remarkably increased RF and MV in freely behaving mice. However, there were no significant differences in breathing parameters between photostimulation of the left and right LPBN (Supplementary Fig. 18d–f). These findings suggest that no pronounced lateralized effects on respiratory function were observed when stimulating the CeA-LPBN circuit.

To further clarify the role of CeA-LPBN circuit in the regulation of anxiety-like behaviors, we employed an optogenetic approach by delivering a virus encoding ChR2 into one side of the CeA and a control virus lacking ChR2 into the contralateral CeA in the same subjects (Supplementary Fig. 19a, b). Behavioral analyses revealed that, with the exception of reduced resting time in the OFT, no significant differences in any parameters of the OFT and EPM were observed between the ChR2-injected side and the ChR2-lacking side when illuminating the axon terminals of CeA^{GABA} neurons projecting to the LPBN (Supplementary Fig. 19c–h). These findings suggested that the activation of CeA-LPBN circuit did not replicate behavioral phenotypes similar to those induced by CeA^{GABA} neuron activation.

Although the activation of CeA-LPBN circuit produced no effect on anxiety-like behaviors, we further investigated whether this circuit regulated breathing patterns through its action on the preBötC. To test this hypothesis, we conducted loss-of-function experiments employing the Flp/FRT system to genetically ablate LPBN neurons projecting to the preBötC. This was achieved by delivering a Cre-dependent AAV vector encoding a genetically engineered Casp3 gene (AAV9-Ef1α-fDIO-taCasp3) into the LPBN. Casp3 activation has been shown to induce cell apoptosis[50]. Concurrently, we introduced a virus encoding ChR2 and a retrograde virus into the CeA and preBötC, respectively (Fig. 6h). For control mice, AAV9-Ef1α-fDIO, which lacks Casp3, was utilized together with other two vectors. Four weeks post-injection, immunohistochemical assays were conducted to confirm the efficiency of neuronal ablation before measuring respiratory parameters. The number of LPBN neurons projecting to the preBötC was markedly reduced in mice injected with the Casp3 vector compared to control mice (Supplementary Fig. 20a–d). Successful ablation resulted in no significant alteration of breathing parameters upon photostimulation of the CeA-LPBN circuit (Fig. 6i–k).

According to the Allen Brain Atlas (http://www.brain-map.org), approximately 90% of LPBN neurons are glutamatergic (LPBN^{Glu}), while the remaining 10% are GABAergic (LPBN^{GABA}). To determine the neurochemical identity of the LPBN neurons involved, we utilized the Cre/LoxP and Flp/FRT systems to selectively ablate either glutamatergic (Fig. 6l and Supplementary Fig. 20e) or GABAergic (Fig. 6p, Supplementary Fig. 20j) LPBN neurons projecting to the preBötC. Four weeks post-injection, the effectiveness of the ablation was validated for both glutamatergic (Supplementary Fig. 20f–i) and GABAergic (Supplementary Fig. 20k–n) neurons before WBP recordings. Ablation of LPBN^{Glu} neurons resulted in no significant changes in breathing parameters upon photostimulation of the CeA^{GABA} neurons projecting to the LPBN projections (Fig. 6m–o), replicating the outcome observed following the ablation of all types of LPBN neuron projecting to the preBötC. In contrast, ablating LPBN^{GABA} neurons did not abolish the photostimulation-evoked increases in RF and MV (Fig. 6q–s). These

https://doi.org/10.1038/s41467-025-58791-6

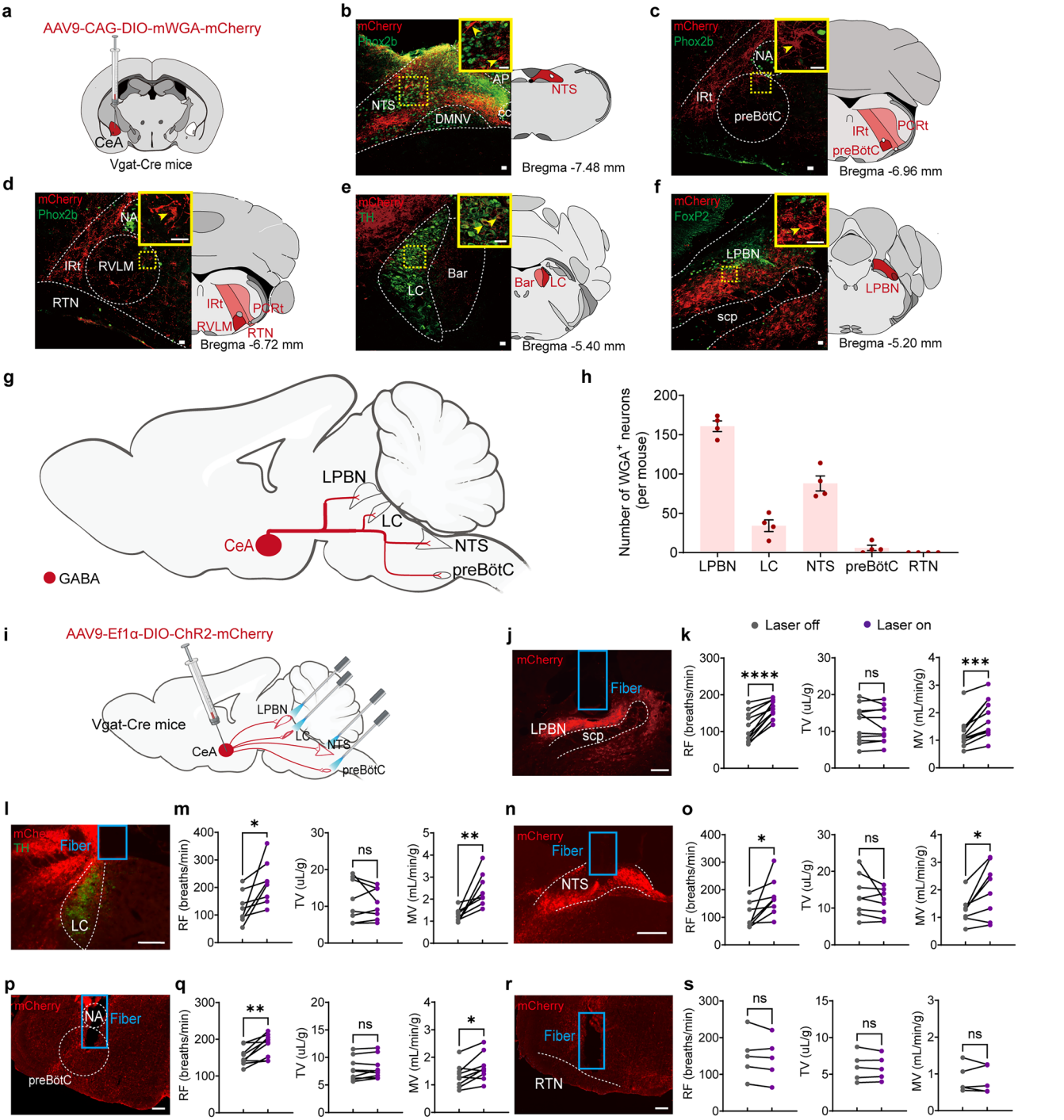

Fig. 5 | Regulation of breathing by activation of CeA^{GABA} neurons projecting to brainstem respiratory centers. a Schematic of the neural tracing strategy by injecting an anterograde virus encoding mWGA to the CeA to identify postsynaptic neurons located in the brainstem. **b**–**f** Representative images showing that postsynaptic neurons of CeA^{GABA} neurons were identified in the LPBN, NTS, LC and preBötC. Scale bars, 20 μm. **g** Summary diagram illustrating primary outputs of CeA^{GABA} neurons in the brainstem. **h** Quantification of the numbers of mWGA^{+} neurons in different brainstem regions ($n = 4$). **i** Schematic of the optogenetic strategy. **j**–**s** Immunohistochemical validation and photostimulation effects on breathing. Typical images showing CeA^{GABA} neuron axons within the LPBN (**j**), LC (**l**), NTS (**n**), preBötC (**p**) and RTN (**r**), as well as fiber traces. Scale bars, 200 μm. Illumination (10 Hz) of the axon terminals of CeA^{GABA} neurons projecting to the LPBN (**k**), LC (**m**), NTS (**o**) and preBötC (**q**) significantly increased RF and MV but not TV using WBP recordings in quiescent mice. $n = 11$ mice for LPBN, $n = 8$ mice for both LC and NTS, $n = 9$ mice for preBötC, $n = 5$ mice for RTN. RF: $p < 0.0001$ for LPBN, $p = 0.0235$ for LC, $p = 0.0384$ for NTS, $p = 0.0059$ for preBötC; MV: $p = 0.0004$ for LPBN, $p = 0.0062$ for LC, $p = 0.0181$ for NTS, $p = 0.0119$ for preBötC. $^{*}p < 0.05$, $^{**}p < 0.01$, $^{***}p < 0.001$, $^{****}p < 0.0001$ by two-tailed paired t-test (**k**, **m**, **o**, **q**, **s**). All data are presented as the mean ± SEM. Source data is provided as a Source Data file. The materials depicted in (**a**, **g**, **i**) are created in BioRender. Xiaoyi, W. (2025) https://BioRender.com/i81e326. Abbreviations: AP area postrema, Bar barrington's nucleus, cc central canal, DMNV dorsal motor nucleus of vagus, IRt intermediate reticular nucleus, LC locus coeruleus, LPBN lateral parabrachial nucleus, NA ambiguous nucleus, NTS nucleus tractus solitarius, PCRt parvicellular reticular nucleus, preBötC preBötzinger complex, RTN retrotrapezoid nucleus, RVLM rostral ventrolateral medulla, scp superior cerebellar peduncle.

https://doi.org/10.1038/s41467-025-58791-6

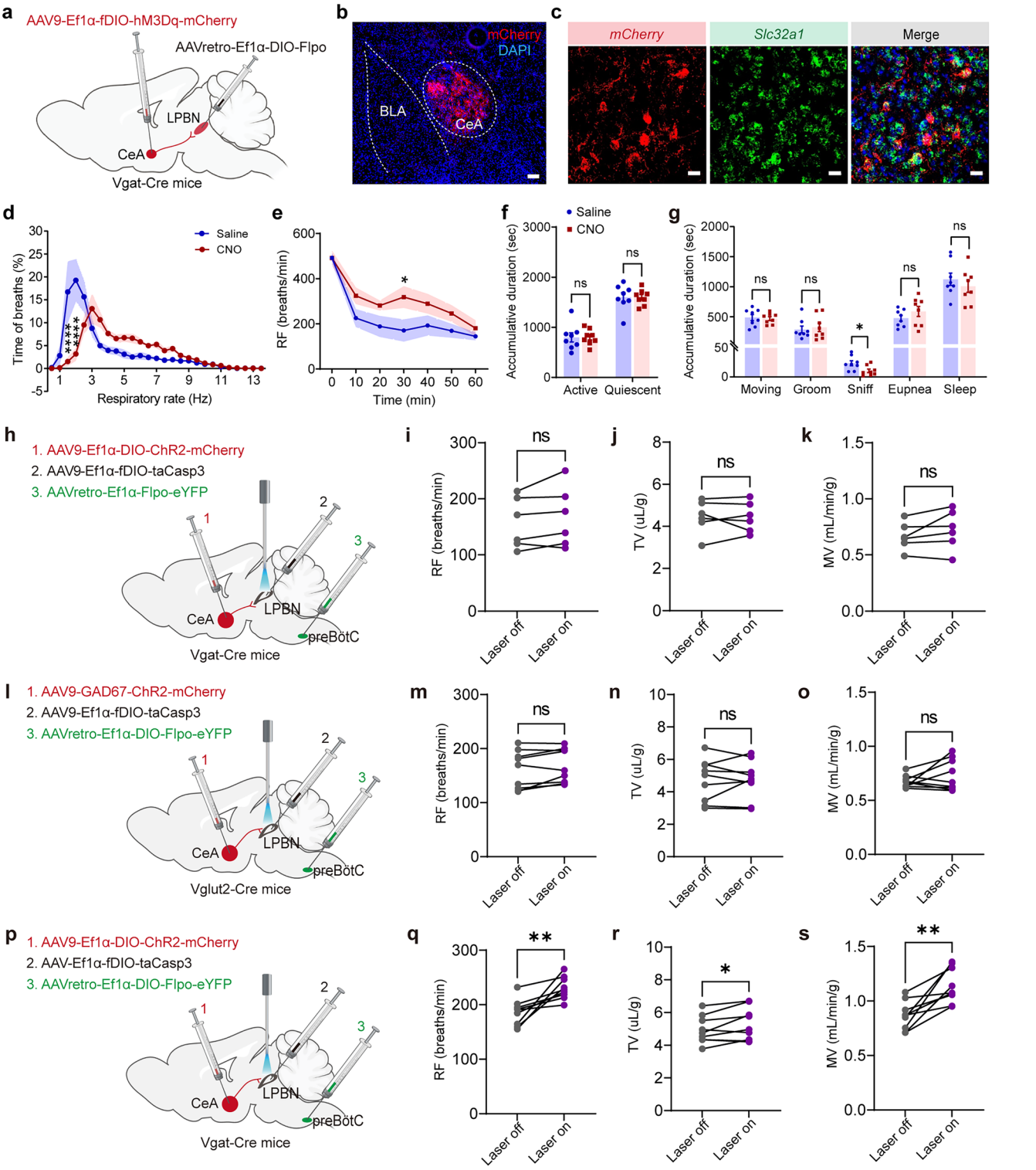

findings suggest that the respiratory changes induced by photostimulation of CeA^{GABA} neurons were most likely mediated by the activation of LPBN^{Glu} neurons projecting to the preBötC.

Activation of CeA^{GABA} neurons differentially regulates electrophysiological activity of LPBN^{Glu} neurons projecting to the preBötC

Having confirmed the respiratory effect of the CeA-LPBN-preBötC circuit, we proceeded to examine whether CeA^{GABA} neurons regulate the electrophysiological properties of LPBN^{Glu} neurons projecting to the preBötC. To achieve this, we injected AAV9-GAD67-ChR2-mCherry into the CeA and AAVretro-EF1α-DIO-eYFP into the preBötC of Vglut2-Cre mice (Fig. 7a). We then assessed the electrophysiological profiles of LPBN^{Glu} neurons projecting to the preBötC in response to photostimulation of CeA^{GABA} neurons projecting to the LPBN (Fig. 7b). Initially, to verify the excitatory effect of ChR2 activation, we performed whole-cell patch clamp slice recordings in CeA^{GABA} neurons, which demonstrated that photostimulation evoked action potentials in a frequency-dependent manner (Fig. 7c). Moreover, immunohistochemical assays and RNAscope-FISH further

Fig. 6 | The CeA-LPBN circuit primarily regulates breathing patterns in behaviorally quiescent state. a Illustration of the viral injection strategy for chemogenetic stimulation of CeA^{GABA} neurons projecting to the LPBN. **b** Immunohistochemical detection of hM3Dq expression in the CeA. Scale bar, 100 µm. **c** RNAscope-FISH images showing colocalization of hM3Dq (red) and *Slc32a1* (green) mRNA in CeA^{GABA} neurons projecting to the LPBN. Scale bars, 20 µm. **d** Distribution of RF (bin size 0.5 Hz) over a 40-min assay of saline and CNO injections ($n = 8$ mice per group). Activation of CeA^{GABA} neurons projecting to the LPBN produced a shift to rapid breaths. $p < 0.0001$ for 1.5 and 2 Hz. **e** Time-course of RF changes over a 60-min recording following saline and CNO injections. RF significantly increased at 30-min mark ($p = 0.0425$). $n = 8$ mice per group. **f** Accumulative duration spent in active and quiescent states during 40-min plethysmography assay ($n = 8$ mice per group). Activation of CeA^{GABA} neurons projecting to the LPBN had no effect on both active and quiescent durations. **g** Accumulative duration of each behavior ($n = 8$ per group). Compared to the saline group, sniff was reduced in the CNO group ($p = 0.0262$). **h** Schematic of the genetic ablation strategy by bilateral injections of a virus encoding Casp3 into the LPBN. **i–k** Following ablation of LPBN neurons projecting to the preBötC, photostimulation (10 Hz) of axon terminals of CeA^{GABA} neurons projecting to the LPBN had no significant effect on breathing parameters ($n = 6$ per group). **l** Schematic illustrating bilateral ablation of $LPBN^{Glu}$ neurons projecting to the preBötC. **m–o** Following ablation of $LPBN^{Glu}$ neurons projecting to the preBötC, photostimulation (10 Hz) of axon terminals of CeA^{GABA} neurons projecting to the LPBN produced no significant effect on breathing parameters ($n = 9$ per group). **p** Schematic of bilateral ablation of $LPBN^{GABA}$ neurons projecting to the preBötC. **q–s** Following ablation of $LPBN^{GABA}$ neurons projecting to the preBötC, photostimulation (10 Hz) of axon terminals of CeA^{GABA} neurons projecting to the LPBN significantly increased ventilation ($n = 9$ for per group). **q**, $p = 0.0045$; **r**, $p = 0.0479$; **s**, $p = 0.0028$. $^{*}p < 0.05$, $^{**}p < 0.01$, $^{****}p < 0.0001$ by two-way ANOVA followed by Šídák's multiple comparisons test (**d**, **e**), two-tailed unpaired *t*-test (**f**, **g**: moving, sniff, eupnea, sleep), two-tailed Mann–Whitney test (**g**: groom) and two-tailed paired *t* test (**i–k**, **m–o**, **q–s**). All data are presented as the mean ± SEM. Source data is provided as a Source Data file. The materials depicted in (**a**, **h**, **l**, **p**) are created in BioRender. Xiaoyi, W. (2025) https://BioRender.com/i81e326.

confirmed the specific expression of ChR2-mCherry in CeA^{GABA} neurons (Fig. 7d–g).

Afterwards, spontaneous firing was recorded in $LPBN^{Glu}$ neurons projecting to the preBötC in brain slices using a cell-attached mode. Based on their firing response to photostimulation of CeA^{GABA} neurons projecting to the LPBN, $LPBN^{Glu}$ neurons were classified into three distinct categories ($n = 41$ neurons from 5 mice): Type 1 neurons with increased firing rate ($n = 6$, Fig. 7h, i), Type 2 neurons with decreased firing rate ($n = 12$, Fig. 7j, k), and Type 3 neurons with unchanged firing rate ($n = 23$, Fig. 7l). Additionally, using whole-cell patch-clamp recordings, we tested changes in spontaneous action potential during photostimulation. The responsive patterns were similar to those observed using the cell-attached mode ($n = 26$ neurons from 5 mice): Type 1 ($n = 3$, Fig. 7m, n), Type 2 ($n = 12$, Fig. 7o, p), and Type 3 ($n = 11$, Fig. 7q). Collectively, these data revealed that activation of CeA^{GABA} neurons projecting to the LPBN produced diverse responses of $LPBN^{Glu}$ neurons projecting to the preBötC.

To further examine whether CeA^{GABA} neurons modulate $LPBN^{Glu}$ neurons projecting to the preBötC through monosynaptic or polysynaptic transmission, we employed the viral strategy as shown in Fig. 7a. Whole-cell patch-clamp recordings were used to capture the inhibitory postsynaptic currents (IPSCs) of fluorescently-tagged $LPBN^{Glu}$ neurons in brain slices (Fig. 7r). Upon delivery of a single pulse of blue light stimulation, IPSCs were evoked in 13 out of 41 neurons (31.7%) (Fig. 7s). Bath application of the sodium channel blocker tetrodotoxin (TTX, 1 µM) abolished the illumination-evoked IPSCs, while the potassium channel blocker 4-aminopyridine (4-AP, 100 µM) reversed the TTX-induced inhibition of IPSCs (Fig. 7t). Additionally, the evoked IPSCs could be completely blocked by the $GABA_A$ receptor blocker picrotoxin (PTX, 50 µM) (Fig. 7u). These results suggest that CeA^{GABA} neurons establish monosynaptic connections with $LPBN^{Glu}$ neurons projecting to the preBötC. Collectively, these electrophysiological assays provide insightful evidence regarding the synaptic mechanisms underlying the observed respiratory effects mediated by the CeA-LPBN-preBötC circuit. Nevertheless, the specific synaptic connections between the LPBN and the preBötC require further investigation due to the complexity introduced by the local circuits formed by both excitatory and inhibitory neurons.

Activation of CeA-PVT circuit regulates anxiety-like behaviors and behavior-related breathing patterns

The regulation of anxiety-like behaviors and breathing patterns by CeA^{GABA} neurons remains a compelling area of investigation. To identify potential circuits involved, we quantified $mWGA^{+}$ neurons in several brain regions, including the periaqueductal gray (PAG), dorsal raphe (DRN), ventral tegmental area (VTA), PVT, lateral habenular nucleus (LHb), and BNST (Fig. 8a–g). Notably, the number of $mWGA^{+}$ neurons was significantly higher in the PVT compared to the other regions surveyed (Fig. 8h).

While the PVT-CeA circuit has been implicated in the modulation of depression behavior[51], stress-related arousal transition[30], and neuropathic pain[52], its role in the regulation of anxiety-like behaviors has been less extensively studied. To address this knowledge gap, we employed the optogenetic technique described above in Vgat-Cre mice (Supplementary Fig. 21a, b). Photostimulation of axonal terminals from CeA^{GABA} neurons projecting to the PVT resulted in a significant decrease in center field time and an increase in resting time during the OFT (Supplementary Fig. 21c–e), as well as reduced EPM open arm entries and time (Supplementary Fig. 21f–h), suggesting the induction of anxiety-like behaviors.

To further investigate whether the activation of the CeA-PVT circuit altered breathing patterns, we employed a chemogenetic approach by injections of two Cre-inducible viral vectors into the CeA and PVT, respectively (Fig. 8i). Immunohistochemical assays and RNAscope-FISH confirmed the expression of hM3Dq in CeA^{GABA} neurons projecting to the PVT (Fig. 8j, k). Our observations revealed that, compared to saline injection, CNO administration significantly increased the number of high-frequency respiratory episodes during 10 to 30 min post-injection (Fig. 8l, m). This effect contrasted with the optogenetic approach, which did not alter breathing parameters due to its short-term stimulation (Supplementary Fig. 21i–k). Additionally, chemogenetic activation of the CeA-PVT circuit was associated with a notable increase in active duration, a decrease in quiescent time, prolonged grooming behavior, and reduced sleep time (Fig. 8n, o). These outcomes demonstrate the important role of CeA-PVT circuit in the regulation of anxiety-like behaviors and behavior-related breathing patterns.

Given that the CeA-PVT and CeA-LPBN circuits differentially regulate anxiety-like behaviors and breathing patterns, the mechanisms by which CeA^{GABA} neurons establish these two circuits remain unclear. We hypothesized that individual CeA^{GABA} neurons might simultaneously target both the LPBN and PVT, thereby coordinating the diverse physiological responses. To test this hypothesis, we utilized an intersectional neural tracing strategy by delivering AAVretro-EF1α-DIO-eYFP into the PVT to label CeA^{GABA} neurons projecting to the PVT. Concurrently, AAV9-EF1α-fDIO-mCherry and AAVretro-EF1α-DIO-flpo were injected into the LPBN and CeA, respectively, to label CeA^{GABA} neurons projecting to the LPBN (Fig. 8p). Immunohistochemical assays were then conducted to identify $eYFP^{+}mCherry^{+}$ (composite color) neurons within the CeA. Quantitative analysis revealed that $mCherry^{+}eYFP^{+}$ neurons accounted for 26.3 ± 5.1% of the total $mCherry^{+}$ neurons and 20.0 ± 3.1% of the total $eYFP^{+}$ neurons (Fig. 8q–s), indicative of divergent axonal projections from individual CeA^{GABA} neurons (Fig. 8t). Additionally, it is also possible that CeA^{GABA}

https://doi.org/10.1038/s41467-025-58791-6

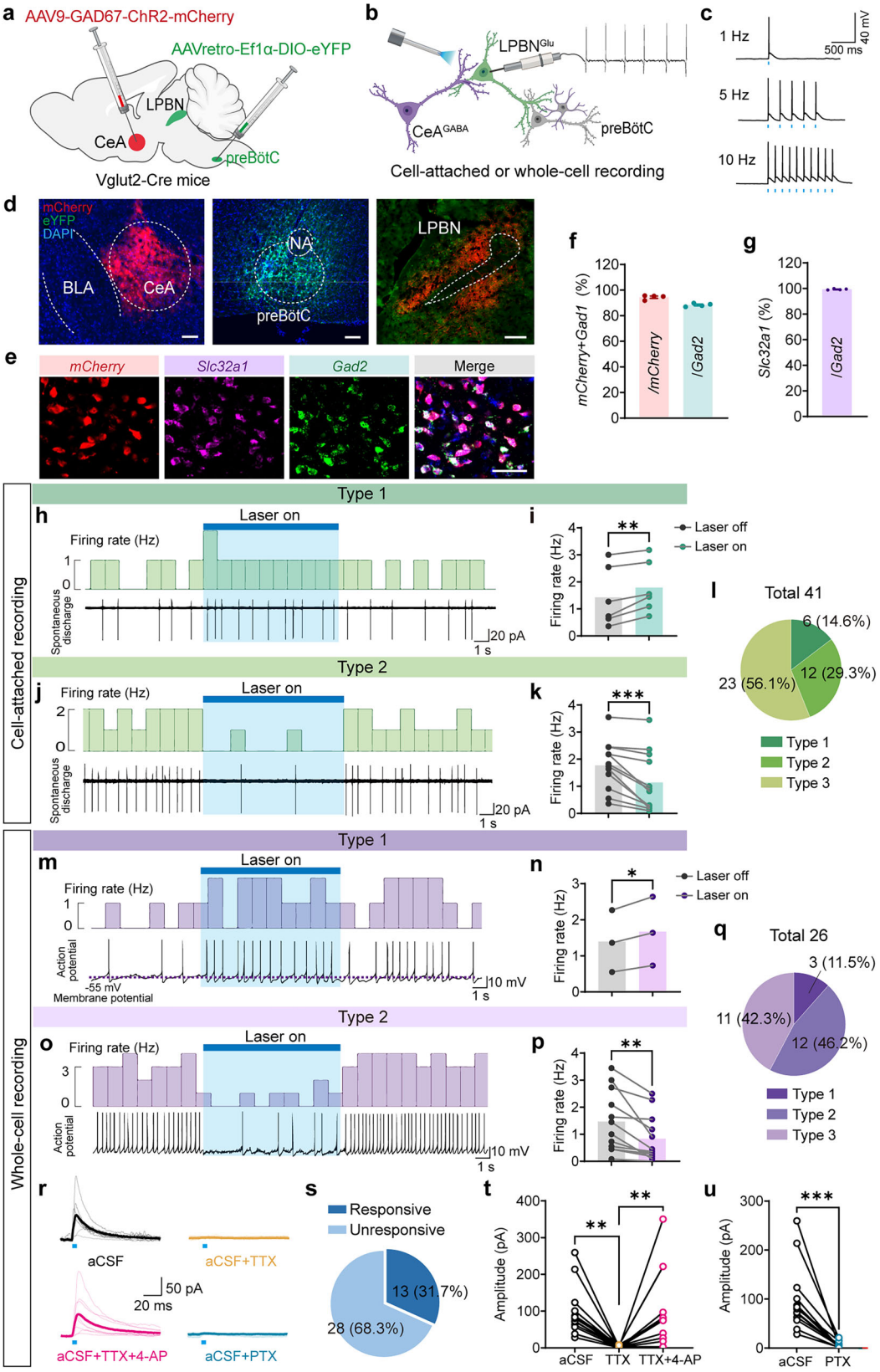

neurons projecting to the PVT and LPBN are distinct subsets, yet they can establish local circuits to regulate behavioral and respiratory patterns (Fig. 8t). Collectively, the neural tracing evidence suggests that this subpopulation of CeA^{GABA} neurons may orchestrate anxiety-like behaviors and behavior-related breathing patterns through their collateral projections to the PVT and LPBN.

Discussion

We demonstrate that ARS not only induces anxiety-like behaviors in mice, but also prolongs active duration, primarily caused by increased grooming time, and simultaneously reduces quiescent time. Alongside these behavioral changes, ARS-treated mice exhibit an increased incidence of high-frequency respiratory episodes. Chemogenetic

Fig. 7 | Photostimulation of CeA^{GABA} neurons produces diverse effects on electrophysiological activity of LPBN^{Glu} neurons projecting to the preBötC. **a**, **b** Schematic of the virus injection strategy and experimental setup for cell-attached and whole-cell patch-clamp slice recordings in LPBN^{Glu} neurons projecting to the preBötC, while illuminating (frequency: 10 Hz; width, 20 ms; power: 20 mW, duration: 10 s) axon terminals of CeA^{GABA} neurons projecting to the LPBN. **c** Action potentials were evoked by photostimulation of ChR2-expressing CeA^{GABA} neurons, as measured by whole-cell patch clamp slice recordings. **d** Immunohistochemical detection of ChR2 expression in the CeA (left, red), eYFP expression in the preBötC (middle, green), and axon terminals of CeA^{GABA} neurons and LPBN neurons projecting to the preBötC (right). Scale bars, 100 μm. **e** RNAscope-FISH images of colocalization of ChR2 (red), *Slc32a1* (pink) and *Gad2* (green) mRNAs in CeA^{GABA} neurons. Scale bar, 50 μm. **f**, **g** Quantitative analysis of the efficiency and specificity of ChR2-mCherry in CeA^{GABA} neurons. $n = 4$ mice. **h**–**k** Example traces showing that photostimulation produced different responsive patterns of firing in two subsets of LPBN^{Glu} neurons projecting to the preBötC (**h**, **j**). Firing rate histograms (10 s bin size; top traces) derived from cell-attached recordings (bottom traces) demonstrate increased firing rates in Type 1 neurons (**i**, $p = 0.0073$, $n = 6$ cells from 5 mice) and decreased firing rates in Type 2 neurons (**k**, $p = 0.0009$, $n = 12$ cells from 5 mice). **l** Pie chart showing the proportion of three subgroups of LPBN^{Glu} neurons projecting to the preBötC based on firing response patterns to photostimulation: Type 1 ($n = 6$, 14.6 %), responsive neurons with increased firing rate; Type 2 ($n = 12$, 29.3%), responsive neurons with decreased firing rate; Type 3 ($n = 23$, 56.1%), unresponsive neurons with unaltered firing rate. $n = 41$ neurons with spontaneous firing from 5 mice. **m**–**p** Typical traces showing changes in action potentials in the presence of illumination (**m**, **o**). Firing rate histograms (10 s bin size; top traces) derived from whole-cell recordings (bottom traces) demonstrate increased firing rates in Type 1 neurons (**n**, $p = 0.0372$, $n = 3$ neurons from 5 mice) and decreased firing rates in Type 2 neurons (**p**, $p = 0.0031$, $n = 12$ neurons from 5 mice). **q** Pie chart showing the proportion of three types of LPBN^{Glu} neurons projecting to the preBötC based on whole-cell recordings ($n = 3$ for Type 1, $n = 12$ for Type 2, $n = 9$ for Type 3, $n = 26$ neurons from 5 mice). **r** Typical traces showing that light-evoked (width: 5 ms, power: 20 mW) IPSCs recorded in LPBN^{Glu} neurons were inhibited by TTX (1 μM). Such an inhibition was reversed by 4-AP (100 μM). The evoked IPSCs were completely eliminated by PTX (50 μM). **s** Pie chart showing the percentage of preBötC-projecting LPBN^{Glu} neurons with light-evoked IPSCs: responsive ($n = 13$ neurons from 5 mice) and unresponsive ($n = 28$ neurons from 5 mice). **t**, **u** Quantification of the amplitude of light-evoked IPSCs of responsive neurons. **t**, $p = 0.0012$, aCSF *vs.* TTX; $p = 0.0098$, TTX *vs.* TTX + 4-AP ($n = 13$ neurons from 5 mice); **u**, $p = 0.0002$ ($n = 13$ neurons from 5 mice). $^{*}p < 0.05$, $^{**}p < 0.01$, $^{***}p < 0.001$ by two-tailed paired *t* test (**i**, **k**, **n**, **p**), two-tailed Wilcoxon matched-pairs signed rank test (**u**), and two-tailed Friedman test with Dunn's multiple comparisons test (**t**). All data are presented as the mean ± SEM. Source data is provided as a Source Data file. The materials depicted in (**a**, **b**) are created in BioRender. Xiaoyi, W. (2025) https://BioRender.com/i81e326.

inhibition of CeA^{GABA} neurons significantly attenuates both behavioral and respiratory changes induced by ARS. Conversely, stimulation of CeA^{GABA} neurons produces behavioral and respiratory changes similar to those observed in ARS-treated mice, characterized by prolonged grooming time and increased high-frequency respiratory episodes. Under conditions of behavioral quiescence or anesthesia, stimulation of CeA^{GABA} neurons also significantly increases central respiratory drive and RF. Furthermore, the activation of the CeA-PVT circuit markedly increases grooming time and high-frequency respiratory episodes, while stimulation of the CeA-LPBN-preBötC circuit significantly enhances ventilation without inducing anxiety-like behaviors. Collectively, these findings suggest that CeA^{GABA} neurons function as a central regulatory hub, orchestrating both anxiety-like behaviors and breathing patterns through distinct circuit mechanisms.

ARS induces anxiety-like behaviors and behavior-related breathing patterns

In humans, the breathing pattern undergoes changes in response to various emotions, such as joy, anger, fear, and anxiety[8,9,53]. For instance, breathing may become rapid and shallow when an individual experiences heightened anxiety, such as during a panic attack[54–56]. Conversely, during moments of calmness and relaxation, there is a tendency for the breathing to slow down and deepen[15,57]. These shifts in breathing patterns are likely linked to the autonomic nervous system's response to different emotional states. Clinical observations have revealed that patients with anxiety or panic disorders exhibit a significantly greater irregularity in TV and RF compared to control subjects. This irregularity is often characterized by a pattern of breathing that includes frequent sighing[13]. These studies suggest that the specific breathing pattern may serve as an important indicator of anxiety.

Here, we utilized a well-established ARS paradigm to induce anxiety-like behaviors in mice, as documented by previous research[30,36,58,59]. Employing this animal model, we elucidated the close relationship between anxiety-like behaviors and behavior-related breathing patterns. We integrated analyses from common behavioral assays, such as the OFT and EPM, with assessments of respiratory waveform, a recently established method[15]. Our behavioral tests revealed that mice displayed anxiety-like behaviors within the first 40 min post-ARS, which subsequently subsided to baseline levels, with almost no signs of anxiety-like behaviors after 40 min. To better understand the temporal dynamics of these behaviors, we proceeded to examine changes in breathing patterns during the first 40 min post-ARS. By analyzing each behavior-related respiratory waveform, we observed that the RF was highest during sniffing, followed by moving, grooming, eupnea, and sleep. This methodology enables us to evaluate the transition between different behaviors based on changes in breathing patterns. In the new cage group, mice exhibited a time-dependent decline in RF, from high levels to normal, within the initial 40-min period after being transferred to the WBP chamber. This change in breathing pattern represents the transition from exploratory to adaptive behavior in the new environment. In contrast, mice in the ARS group maintained higher RF levels between the 20- and 30-min marks after placement in the WBP chamber, returning to normal RF levels after 40 min. Analysis of the 40-min WBP data revealed that, on average, ARS exposure resulted in a significant increase in grooming and eupnea time, and a decrease in sniffing and sleep time. Specifically, during the initial 5 min post-ARS, there was a greater increase in grooming time and a larger decrease in moving and sniffing time, resulting in a lower RF in ARS mice compared to their control counterparts. Between 20- and 30-min post-ARS, ARS mice exhibited a higher RF than control mice, most likely due to increased grooming time. Therefore, we suggest that ARS-exposed mice spend more time grooming and less time sniffing, leading to a pronounced increase in high-frequency respiratory episodes.

Both grooming and sniffing are adaptive behaviors that serve as indicators of anxiety-like behaviors in rodents. Grooming is an evolutionarily conserved repetitive behavior characterized by a complex sequenced structure involving repeated stereotyped movements, sequentially from paw and nose, to the face, to the head and finally ending with body licking[60–62]. The emotional impact of grooming remains a subject of debate. Some studies suggest that self-grooming is associated with post-stress anxiety alleviation or self-soothing, thus potentially alleviating anxiety-like behaviors[58,63,64]. Conversely, other reports demonstrate that grooming can occur concurrently with anxiety, particularly in the case of excessive grooming, which has been linked to heightened anxiety levels[65,66]. These perspectives indicate that the grooming behavior serves as an indicator or a modulator of anxiety-like behaviors in rodents. In the present study, we propose that grooming functions not only as an indicator but also as an emotional modulator of ARS-induced anxiety-like behaviors.

Sniffing is a specialized respiratory behavior that enables rodents to localize and track objects in their environment. This behavior is precisely and strongly modulated as a function of task demands,

https://doi.org/10.1038/s41467-025-58791-6

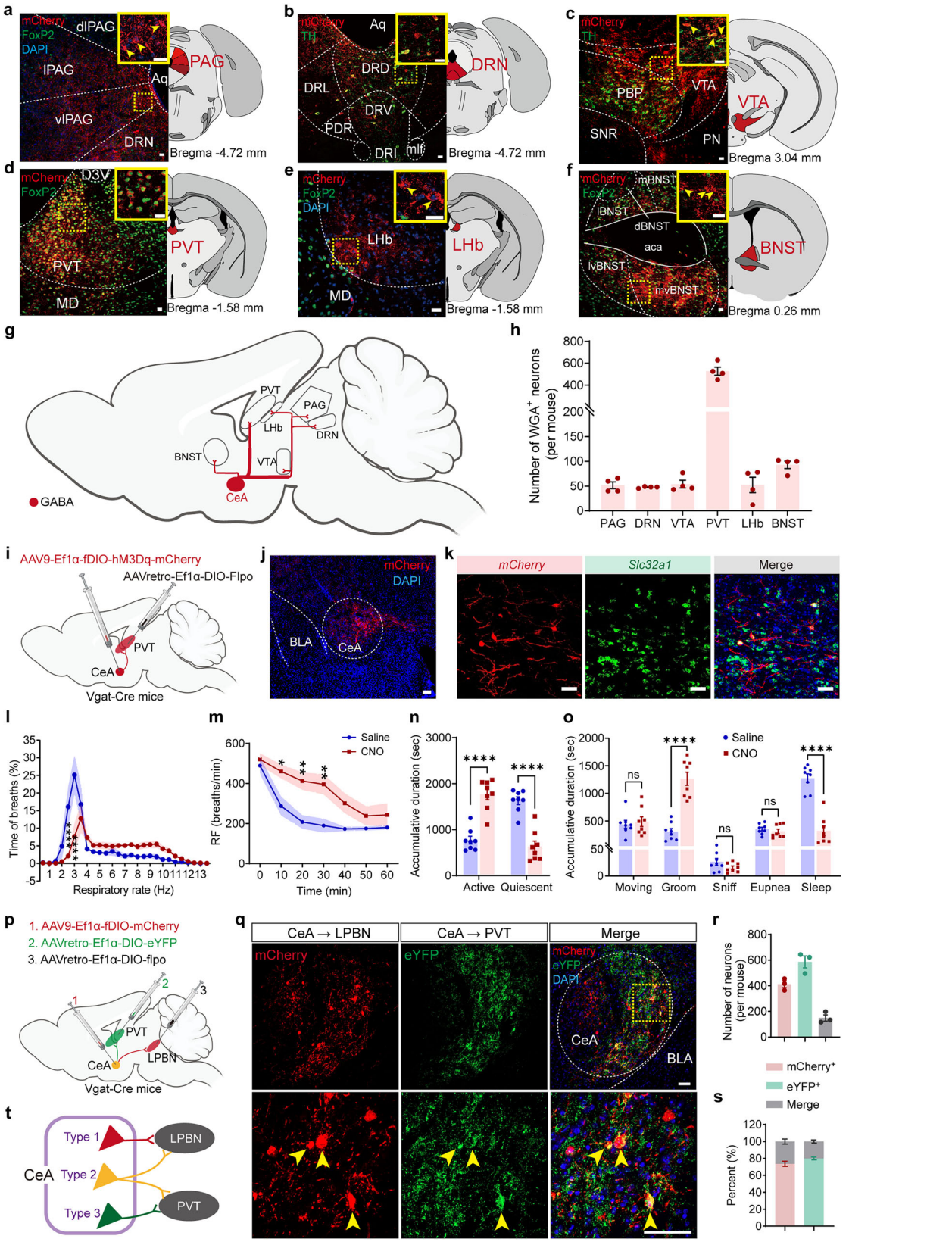

behavioral state, and stimulus context[67,68]. When mice enter a new environment, they often engage in sniffing to explore the unfamiliar surroundings, which can help reduce anxiety by providing sensory stimulation and promoting a sense of control over their surroundings[69]. By contrast, edge-sniff is significantly reduced in rodents exhibiting anxiety-like behaviors[43]. Consistent with this observation, we noted a significant decrease in sniffing time in ARS-treated mice, suggesting a clear association between sniffing and anxiety-like behaviors. Altogether, rodents exhibiting anxiety-like behaviors are consistently accompanied by abnormal grooming and sniffing, implying that both behaviors and their specific breathing patterns serve as important indicators of anxiety.

Fig. 8 | Respiratory and behavioral changes after activation of the CeA-PVT circuit. a–**g** Neural tracing analysis of downstream targets of CeA^{GABA} neurons by delivering a virus encoding mWGA into the CeA from Vgat-Cre mice. Postsynaptic neurons of CeA^{GABA} neurons were detected in several brain regions involved in emotional control. Scale bars, 20 μm. **h** Quantification of the number of $mWGA^+$ neurons in different regions ($n = 4$ mice). **i** Schematic of the chemogenetic strategy to specifically activate CeA^{GABA} neurons projecting to the PVT. **j** Immunohistochemical detection of hM3Dq-mCherry expression in the CeA. Scale bar, 100 μm. **k** RNAscope-FISH images showing colocalization of hM3Dq (red) and *Slc32a1* (green) mRNA. Scale bars, 50 μm. **l** Distribution of RF (bin size 0.5 Hz) in a 40-min assay following saline and CNO injections ($n = 8$ mice per group). Activation of LPBN-projecting CeA^{GABA} neurons produced a shift to rapid breaths. $p < 0.0001$ for 2.5 and 3 Hz. **m** The injection of CNO (i.p.) significantly increased RF at 10-, 20- and 30-min mark compared to saline treatment. $n = 8$ mice per group. 10 min, $p = 0.0159$; 20 min, $p = 0.0024$; 30 min, $p = 0.0022$. **n** Accumulative duration spent in active and quiescent states during 40-min plethysmography recordings. Activation of CeA^{GABA} neurons produced prolonged active time and reduced quiescent periods. **o** Accumulative duration of each behavior. **p** Schematic of the neural tracing strategy to identify CeA^{GABA} neurons that concurrently target both the PVT and LPBN. **q** Representative images showing identification of CeA^{GABA} neurons projecting to the LPBN (red) and PVT (green), and their overlap (composite color). The view indicated by yellow dashed rectangle (top) was enlarged in bottom images. Scale bars, 50 μm. **r** Quantification of the number of $mCherry^+$, $eYFP^+$ and overlap neurons ($n = 3$ mice). **s** Quantitative analysis of overlap neurons accounted for 26.3% ± 5.1% of the total $mCherry^+$ neurons and 20.0% ± 3.1% of the total $eYFP^+$ neurons ($n = 3$ mice). **t** Schematic of architecture of CeA^{GABA} neurons that form the CeA-PVT and CeA-LPBN circuits. $^*p < 0.05$, $^{**}p < 0.01$, $^{****}p < 0.0001$ by two-way ANOVA followed by Šídák's multiple comparisons test (**l, m**), two-tailed unpaired *t* test (**n**, **o**). All data are presented as the mean ± SEM. Source data are provided as a Source Data file. The materials depicted in (**g**, **i**, **p**) are created in BioRender. Xiaoyi, W. (2025) https://BioRender.com/i81e326. Abbreviations: aca anterior commissure, anterior part Aq aqueduct, D3V dorsal 3rd ventricle, dlPAG dorsolateral periaqueductal gray, DRD dorsal raphe nucleus, dorsal part, DRI dorsal raphe nucleus, interfascicular part, DRL dorsal raphe nucleus, lateral part, DRN dorsal raphe nucleus, DRV dorsal raphe nucleus, ventral part, lBNST nucleus of stria terminalis, lateral division, LHb lateral habenular nucleus, lPAG lateral periaqueductal gray, lvBNST nucleus of stria terminalis, lateralventral division, mBNST nucleus of stria terminalis, medial division, MD mediodorsal thalamic nucleus, mlf medial longitudinal fasciculus, mvBNST nucleus of stria terminalis, medialventral division, PBP parabrachial pigmented nucleus of the ventral tegmental area, PN paranigral nucleus, PVT paraventricular thalamic nucleus, SNR substantia nigra, reticular part, vlPAG ventrolateral periaqueductal gray, VTA ventral tegmental area.

Clinical observations suggest that individuals with anxiety-related disorders frequently experience poor sleep quality, including disturbances like insomnia[70]. Zhao and colleagues have reported that ARS-induced anxiety could heighten wakefulness modulated by the PVT to CeA pathway[30]. In line with these data, our study also demonstrates a decrease in sleep duration in ARS-treated mice, providing a potential link between sleep and anxiety-like behaviors.

Collectively, we demonstrate that ARS-induced anxiety-like behaviors were associated with abnormal grooming and sniffing, as well as distinct breathing patterns, including increased high-frequency respiratory episodes. These outcomes not only provide a theoretical basis for behavioral/emotional regulation of breathing, but also supply a foundation for respiratory phenotypes in psychiatric disorders.

Contribution of CeA^{GABA} neurons to regulating anxiety-like behaviors and breathing patterns

Accumulating evidence suggests the existence of an emotional respiratory system, wherein the emotional and respiratory systems are integrated within the brain. It has been hypothesized that respiratory rhythms generated in the limbic system constitute the fundamental rhythms associated with the activation of emotions[9]. This perspective posits that emotional changes are coupled with the generation of specific respiratory rhythms and patterns, thereby highlighting the intricate relationship between emotional states and respiratory function.

In the present study, we demonstrate that the activation level of CeA^{GABA} neurons was significantly elevated during the ARS. Behavioral tests revealed that chemogenetic inhibition of CeA^{GABA} neurons alleviated anxiety-like behaviors in ARS-treated mice; photostimulation of CeA^{GABA} neurons alone was sufficient to trigger anxiety-like behaviors. Analysis of WBP data indicated that chemogenetic inhibition of CeA^{GABA} neurons significantly reduced ARS-induced prolonged grooming time and high-frequency respiratory episodes. Conversely, chemogenetic stimulation of CeA^{GABA} neurons prolonged grooming time and increased the incidence of high-frequency respiratory episodes. Additionally, in vivo Ca^{2+} signal recordings indicated that heightened CeA^{GABA} neuron activity coincided with the onset of grooming and increased RF. Given recent reports that highlight the dual role of CeA neurons in regulating self-grooming and post-stress anxiety[58,71], our findings suggest that the high-frequency respiratory episodes observed in anxiety-like behaviors, whether induced by ARS or stimulation of CeA^{GABA} neurons, may partially result from the prolonged grooming time in mice. However, due to the lack of respiratory pattern measurements and behavioral tests during ARS, the anxiety model presented in the present study largely represents post-stress respiratory patterns and does not fully capture the breathing patterns characteristic of the most anxious state.

Clinical observations have documented central apnea elicited by amygdala stimulation observed in epilepsy patients[72], and structural deficiency of amygdala in patients with obstructive sleep apnea[73]. These studies raise the important questions regarding the role of CeA^{GABA} neurons in regulating breathing under behaviorally quiescent conditions (e.g., eupnea and sleep). Specifically, it remains poorly understood whether stimulation of CeA^{GABA} neurons during behavioral quiescence still induces similar respiratory phenotypes. Using WBP measurements, we demonstrate that photostimulation of CeA^{GABA} neurons in behaviorally-quiescent mice significantly increased RF and MV, without significant change in the number of sighs or apneas. Moreover, in anesthetized mice, photostimulation of these neurons also potentiated central respiratory drive. Combining these data, we suggest the presence of specific neural circuits connecting the CeA to respiratory centers in the brainstem, which mediate the regulation of breathing patterns by CeA^{GABA} neurons. These results underscore the complex interplay between the CeA and respiratory control mechanisms and propose the potential pathways through which CeA^{GABA} neurons influence respiratory function under both active and quiescent conditions.

CeA^{GABA} neurons orchestrate anxiety-like behaviors and breathing patterns through specific neural circuits

As demonstrated herein, the activation of CeA^{GABA} neurons elicits anxiety-like behaviors along with behavior-related respiratory patterns. Whether these effects are mediated by overlapping or distinct neural circuits remains an open question. Our neural tracing results revealed a broad network of projections from CeA^{GABA} neurons, encompassing regions involved in emotional processing such as the BNST, LHb, VTA, and PVT, as well as brainstem nuclei involved in respirator control, including the LPBN, LC, NTS, and preBötC, corroborating previous reports[34,74]. Based on quantitative analysis, which identified a substantial number of postsynaptic neurons of CeA^{GABA} neurons in the PVT, we focused on the role of CeA-PVT circuit. Behavioral tests revealed that photostimulation of CeA^{GABA} neuron axon terminals within the PVT elicited anxiety-like behaviors indistinguishable from those evoked by direct illumination of the CeA. Additionally, analysis of WBP data indicated that chemogenetic stimulation of the CeA-PVT circuit significantly increased both grooming time and high-

frequency respiratory episodes. Therefore, the CeA-PVT circuit plays a primary role in the regulation of anxiety-like behaviors.

Beyond the aforementioned CeA-PVT circuit, we extended our investigation to include respiratory control centers in the brainstem. Photostimulation of CeA^{GABA} neuron axon terminals targeting brainstem regions, such as the LPBN, LC, NTS, and preBötC, notably increased pulmonary ventilation in quiescent mice and enhanced central respiratory drive in anesthetized mice, suggesting that CeA^{GABA} neurons modulate breathing through diverse brainstem circuits. We propose that these circuits orchestrate respiratory control with different behavioral states. In essence, different outputs of the CeA may influence emotion-specific breathing patterns. Further investigations are required to clarify the physiological functions that engage the aforementioned brainstem circuits.

Given the pivotal role of the LPBN in modulating breathing patterns[5], we concentrated our efforts on delineating the contribution of the CeA-LPBN-preBötC circuit in this regulation. In addition to neural tracing evidence and gain-of-function data presented above, our loss-of-function experiments demonstrated that the ablation of $LPBN^{Glu}$ neurons projecting to the preBötC eliminated enhanced ventilatory response evoked by photostimulation of CeA^{GABA} neuron axon terminals targeting the LPBN. Furthermore, electrophysiological data revealed that photostimulation of axon terminals of CeA^{GABA} neurons projecting to the LPBN produced either excitatory or inhibitory effects on spontaneous firing activity in different subgroups of $LPBN^{Glu}$ neurons projecting to the preBötC. These effects were most likely achieved through the recruitment of microcircuits within the LPBN. Further studies are needed to fully elucidate the specific pathways and synaptic mechanisms involved in the CeA-LPBN-preBötC circuit and its role in respiratory control. Dissection of these circuits will provide a more comprehensive understanding of the neural circuits underlying respiratory function. However, photostimulation of axon terminals of CeA^{GABA} neurons projecting to the LPBN generated no anxiety-like behaviors. Based on these observations, we propose that the CeA-LPBN circuit primarily mediates the control of breathing patterns rather than anxiety-like behaviors.

As discussed above, while the CeA-LPBN-preBötC and CeA-PVT circuits differentially influence the regulation of anxiety-like behaviors and breathing patterns, it is important to note that both circuits may contribute to the control of other physiological functions when considering the structural and functional complexity of the CeA. Although many studies have elucidated the significance of PVT-CeA circuit, the function of CeA-PVT circuit remains less understood. Our findings reveal the critical contribution of this circuit to regulating anxiety-like behaviors and behavior-related breathing patterns. The CeA-LPBN pathway has been extensively investigated and is known to modulate key behaviors such as food intake, alcohol consumption, pain responses, and aversion. Given the established influence of the CeA-LPBN circuit on these behaviors, it is plausible that this circuit also plays a role in modulating breathing patterns associated with these physiological processes.

Nevertheless, it is important to elucidate how CeA^{GABA} neurons locally organize the CeA-PVT and CeA-LPBN circuits. These neurons may be identical or distinct populations. Our neural tracing evidence has identified a subset of CeA^{GABA} neurons that simultaneously innervate both the PVT and LPBN through collateral branching, enabling multi-target innervation. As reported before[75], this anatomical arrangement allows single neurons to form synaptic connections with a diverse set of neurons spanning multiple regions. In the present study, the multi-target projection pattern potentially enables these neurons to concurrently deliver signals to coordinate anxiety-like behaviors and diverse breathing patterns. This insight extends our understanding of how the CeA orchestrates behavioral states alongside respiratory function, as well as other autonomic processes. However, it is also conceivable that two distinct subpopulations of CeA^{GABA} neurons might be independently orchestrating these functions through local circuits. Liu et al. have proposed that LPBN neurons can simultaneously modulate breathing and pain by engaging two anatomically discrete yet interconnected core and shell subpopulations, which branch out towards limbic systems and respiratory centers in the medulla[76]. This hypothesis aligns with the possibility that separate groups of CeA^{GABA} neurons project to the PVT and LPBN without any intersection of their pathways. Interactions among these neurons could be facilitated by intricate microcircuits within the CeA itself.

We demonstrate here that both ARS treatment and separate stimulation of the CeA^{GABA} neurons elicit anxiety-like behaviors alongside behavior-specific breathing patterns. The CeA^{GABA} neurons, serving as a central hub, are instrumental in orchestrating anxiety-like behaviors and breathing patterns through the CeA-PVT and CeA-LPBN-preBötC circuits, correspondingly (Supplementary Fig. 22). These insights may offer a theoretical framework for the behavioral and emotional modulation of respiration and lay groundwork for diagnosing psychiatric conditions by evaluating respiratory symptoms.

Methods

Animals

Vgat-Cre (*Slc32a1*$^{tm2(cre)Lowl}$, JAX016962, Jackson Laboratories, USA), Vglut2-Cre (*Slc17a6*$^{tm2(cre)Lowl}$, JAX016963, Jackson Laboratories, USA) and C57BL/6J (Beijing Vital River Laboratory Animal Technology, Beijing, China) mice were used in this experiment. The experiments were conducted in 8- to 12-week-old mice of either sex, unless otherwise specified. Detailed information regarding the sex of mice has been provided in Supplementary Table 1. The mice were housed under program-controlled temperature (24 ± 1 °C) and humidity (50% ± 10%) with a fixed 12 h: 12 h light: dark cycle (beginning at 7:00 a.m.) and with *ad libitum* access to food and water. Age-balanced littermate mice were randomly assigned to experimental groups. All behavioral tests were conducted during the light phase. In the behavioral tests, the mice were allowed to adapt to laboratory conditions for ~1 week and to habituate to the testing situation for at least 2 h before experiments. Biohazard wastes were managed following the Medical Waste Management Regulations of China. All experiments were carried out under the Guide for the Care and Use of Laboratory Animals and were approved by the Animal Care and Ethical Committee of Hebei Medical University.

Acute restraint stress model

xperimental mice were taken from home cage, gently placed into a small and transparent tube (3 cm diameter and 10 cm length) with holes opened on the top for ventilation, and maintained in this restraint for 30 min. The control group was taken from the home cage and placed in a new cage for 30 min. Mice were consecutively monitored to ensure proper ventilation. After the 30-min restraint in the tubes or a new cage treatment, mice were transferred into the WBP chamber for respiratory function tests. For the behavioral tests, the mice were allowed to return to their home cages for 15, 30, 40, 50 or 60 min before undergoing the behavioral tests.

Breathing measurements

The ventilatory response was measured using WBP (EMKA Technologies or DSI/Buxco) as described previously[77,78]. A mass flow regulator provided quiet, constant, and smooth air mixture (0.5 L/min) throughout the WBP chamber (volume: 480 mL). The temperature and humidity in the chamber were continuously monitored and used to correct TV breath by a breath basis. Mice were placed into chambers individually and all plethysmography experiments were video-recorded. Video of behaviors, plethysmography traces and breathing parameters, comprising RF (breaths/min), TV (μL/g), and MV (μL/min/g), were recorded and measured simultaneously. According to

different experimental purposes, we designed three experimental protocols: (1) to measure the response of post-stress breathing pattern and ventilatory parameters in mice, the animals were first allowed to acclimate in the chamber individually for 60 min to minimize the effects of the novel environment on breathing patterns and parameters. After acclimation, the experimental group underwent 30 min of restraint stress, while the control group was transferred into a new cage for 30 min. After the respective treatments, 40-min lung function measurements were taken by placing the animals back into the WBP chambers. Starting from 0 min, the respiratory parameters were analyzed by averaging 1-min intervals every 10 min; (2) to verify the effects of activation or inhibition of neurons on behavioral breathing, building on the first experimental protocol, we administered saline or CNO (i.p.) 30 min prior to the start of new cage or restraint treatment during the acclimatization process. The subsequent steps remained consistent with the previous procedure; (3) to investigate the effects of activation or inhibition of neurons on breathing physiologically, excluding the effects of behavioral factors, the mice were placed in the chamber prior to an experimental protocol for at least 60 min, thereby minimizing the potential influences of a novel environment that could induce additional behavioral responses affecting respiration. After acclimation, mice were received intraperitoneal injections of either saline or CNO. Their respiratory activity was then monitored in the chamber for at least 4 h.

Ventilatory flow signals were recorded, amplified, digitized, and analyzed using IOX 2.10 (EMKA Technologies) and FinePointe (DSI, USA) to determine the ventilatory parameters over sequential 60-s epochs (150–200 breaths). In some cases, raw respiratory waveform data were processed off-line and analyzed using Spike 2 software (Cambridge Electronic Design). Animal behavioral analysis was based on the video recorded during lung function test, to precisely match the respiratory waveforms, dividing into movement, groom, sniff, eupnea, and sleep (The sleep waveforms were verified using an Electroencephalogram, as depicted in Supplementary Movie 2). All behavioral analyses were made from 0 to 40 min. TV and MV were normalized to body weight (grams). MV was calculated as the product of the RF and TV. An apneic event was defined as three or more missed breaths or a breath-holding duration longer than 1.2 s. Sighs were identified based on their characteristic large amplitude (2× tidal volume). Note that spontaneous apneas and post-sigh apneic events were analyzed separately.

Virus injection and optical fiber implantation

All viral injections were performed using previously described procedures[78,79]. Briefly, mice were anesthetized with pentobarbital sodium (60 μg/g, i.p.). Additional anesthetic was administered as needed (30% of the original dose, i.p.). The depth of anesthesia was assessed by a lack of corneal and hind-paw withdrawal reflexes every 30 min. All surgical procedures were executed under strict aseptic conditions. Each mouse was placed in a prone position on a stereotaxic device (RWD Life Science, China), while the body temperature was maintained at 37 °C using a program-controlled heating pad. The eyes were covered with ophthalmic ointment to prevent drying. Injections were conducted using a virus-filled glass pipette (approximately 25 μm tip diameter) connected to a syringe pump (Harvard Apparatus, USA). After exposing the skull and drilling a small hole, the glass micropipette was positioned above the CeA (anterior-posterior (AP), −0.8 mm; medial-lateral (ML), ±2.65 mm; dorsal-ventral (DV), −4.68 mm), LPBN (AP, −5.22 mm; ML, ±1.45 mm; DV, −3.50 mm), preBötC (AP, −7.18 mm; ML, ±1.38 mm; DV, −5.85 mm), PVT (AP, −0.80–1.20 mm; ML, 0 mm; DV, −3.05 mm). The stereotaxic coordinates refer to *The Mouse Brain in Stereotaxic Coordinates*[80]. Virus was unilaterally or bilaterally injected into the nuclei at 50 nL/min using the microsyringe pump controller. All unilateral manipulations were counterbalanced across experimental sessions. We randomly alternated the side (left or right) for each animal to ensure equal use of both sides throughout the experiment. The pipette was retained for at least 5 min before withdrawal. After that, each mouse received injections of the antibiotic ampicillin (125 mg/kg, i.p.) and the analgesic ketorolac (4 mg/kg, i.p.). They were then allowed to recover for 3–4 weeks until resuming normal activity before the next experimental measurements were taken.

Viral vectors were purchased from Shanghai Genechem or Brain Case. All viral titers were >10^{12} GC/mL and stored in aliquots at −80 °C until use.

For in vivo fiber photometry, 80 nL of AAV9-Ef1α-DIO-GCaMP6m was unilaterally injected into the CeA of Vgat-Cre mice. Three weeks after injection, an optical fiber (outer diameter (OD), 200 μm; numerical aperture (NA), 0.37; purchased from Sansh Technology) was implanted above the injection site.

For chemogenetic experiments, 80 nL of AAV- Ef1α-DIO-hM4Di-eYFP or AAV9-Ef1α-DIO-hM3Dq-mCherry were bilaterally injected into the CeA. For control experiments, 80 nL of AAV9-Ef1α-DIO-eYFP was used instead of hM4Di or hM3Dq. For chemogenetic projection-specific activation of LPBN- or PVT-projecting CeA^{GABA} neurons, 100 nL of AAVretro-Ef1α-DIO-Flpo was injected in the LPBN or PVT of Vgat-Cre mice. Meanwhile, 100 nL of AAV9-Ef1α-fDIO-hM3Dq-mCherry was injected in the CeA to transfect LPBN- or PVT-projecting CeA^{GABA} neurons with hM3Dq.

For local optogenetic stimulation, 80 nL of AAV9-Ef1α-DIO-ChR2-mCherry or AAV9-Ef1α-DIO-eNpHR3.0-eYFP (80 nL) was unilaterally injected into the CeA. AAV9-Ef1α-DIO-eYFP was used as controls. Three weeks after injections, an optical fiber (OD, 200 μm; NA, 0.22) was placed above the CeA bilaterally. For optogenetic manipulation of the CeA axonal terminals, we injected AAV9-Ef1α-DIO-ChR2-mCherry (80 nL) into the CeA unilaterally. AAV9-Ef1α-DIO-eYFP (80 nL) was used as controls. 3 weeks after injection, an optical fiber (OD, 200 μm; NA, 0.22) was implanted above the LPBN (AP, −5.22 mm; ML, ±1.45 mm; DV, −3.50 mm), LC (AP, −5.51 mm; ML, ±0.85 mm; DV, −3.25 mm), NTS (AP, −7.30 mm; ML, ±0.5 mm; DV, −4.40 mm), preBötC (AP, −7.18 mm; ML, ±1.38 mm; DV, −5.85 mm), RTN (AP, −6.75 mm; ML, ±1.55 mm; DV, −5.93 mm) or PVT (AP, −1.00 mm; ML, 0 mm; DV, −3.05 mm) ipsilaterally.

For ablation of specific circuit of LPBN neurons projecting to the preBötC, 80 nL of AAV9-Ef1α-fDIO-taCasp3 and 60 nL of AAVretro-Ef1α-Flpo-eYFP were injected into the LPBN and preBötC of Vgat-Cre mice, respectively. AAV9-Ef1α-DIO-ChR2-mCherry (80 nL) was injected into the CeA simultaneously. Three weeks after injections, an optical fiber (OD, 200 μm; NA, 0.22) was placed above LPBN to illuminate CeA^{GABA}-LPBN terminals. Similarly, 80 nL of AAV9-Ef1α-fDIO-taCasp3 and 60 nL of AAVretro-Ef1α-DIO-Flpo-eYFP were used to ablate $LPBN^{Glu}$ neurons projecting to the preBötC, and AAV9-GAD67-ChR2-mCherry (80 nL) was injected into CeA of Vglut2-Cre mice to transfect CeA^{GABA} neurons. AAV9-Ef1α-fDIO-taCasp3 and AAVretro-Ef1α-DIO-Flpo-eYFP were used to ablate $LPBN^{GABA}$ neurons projecting to the preBötC, and AAV9-Ef1α-DIO-ChR2-mCherry was injected into CeA of Vgat-Cre mice.

For anterograde tracing, 60 nL of AAV9-CAG-DIO-mWGA-mCherry or AAV9-Ef1α-DIO-mCherry was injected into the CeA unilaterally. For projection-specific retrograde labeling strategy, 80 nL of AAVretro-Ef1α-DIO-eYFP was injected into the PVT to label PVT-projecting CeA^{GABA} with eYFP. Simultaneously, 60 nL of AAV9-Ef1α-fDIO-mCherry and 80 nL of AAVretro-Ef1α-DIO-Flpo were used to label LPBN-projecting CeA^{GABA} with mCherry.

For the manipulation of CeA^{Glu} neurons, AAV9-vglut1-hM3Dq-mCherry (80 nL) was injected into the CeA of C57BL/6J mice for chemogenetics, AAV9-vglut1-ChR2-mCherry (80 nL) for optogenetics and AAV9-vglut1-eYFP (80 nL) for control animals.

Behavioral test

Behavioral testing was performed during the dark phase, under red light. Animals were placed in the testing area before the test for at least

2 h for acclimation. The facilities of behavioral test were cleaned to eliminate residual odor from previous experiments before the test. While each mouse went through different tests, they were never submitted to the same experiment for less than 1 week. For the optogenetic experiments, an optical fiber fixed in the mouse's brain was connected to a patch cord. Subsequently, the mice were put back into the home cage for at least 10 min and then introduced to the arena for the experiments.

OFT

The open field arena was a square box (50 × 50 cm) with opaque plexiglas walls within a sound attenuated room. Each test mouse was placed in the center of the box and was allowed to freely explore its surroundings, recorded by a camera attached to a computer. The movement was automatically tracked and analyzed by Smart v3.0 small animal behavior video recording and analysis system (Version 3.0, Panlab, Spain). The time spent in the center area, resting time, and total distance traveled were measured. To assess the effect of optogenetic activation on locomotor activity, mice were tested for a 10-min session, controlled by stimulation of null-ChR2 virus injection.

EPM test

To measure anxiety-like behavior, a plus-shaped maze with two 30 cm long opposite closed arms, two 30 cm long opposite open arms, and a central square of 5 cm sides was situated 50 cm above the floor. The test mouse was placed in the open arm adjacent to the center and freely explored the maze for 10 min. Entries into open arms, time spent in open arms, and total distance traveled were calculated by Smart v3.0.

Fiber photometry

To record Ca^{2+} fluorescence of CeA^{GABA} neurons, AAV9-Ef1α-DIO-GCaMP6m was unilaterally injected into CeA and an optic fiber was placed into the CeA ipsilaterally 3 weeks after injection. Photometric recordings were conducted using the single-channel fiber photometry recording system (ThinkerTech) 1 week after the fibers-implantation procedures to ensure adequate animal recovery. We obtained calcium-dependent fluorescence signals by stimulating neurons expressing GCaMP6m with laser intensities for the 470 nm wavelength bands (30–50 μW), and 410 nm signal (20 μW) was further used to correct movement artifacts. Light emission was recorded using an sCMOS Camera, and the values of Ca^{2+} signal changes (ΔF/F) by calculating (F − F0)/F0 (Averaged baseline fluorescence signal recorded) were analyzed by MATLAB.

Mice were placed in the testing environment (their home cage or WBP chamber) 60 min prior to the beginning of recording (for adaptation). To measure the temporal dynamic activities of CeA neurons in response to ARS exposure, we monitored the Ca^{2+} activity of CeA^{GABA} neurons during restraint treatment, or entries into a new cage as a control condition. A 30-s window around the beginning of restraint was analyzed, with the period 10 s before stimulus onset taken as baseline. Ca^{2+} responses during the first time of restraint procedure of each mouse were analyzed.

To examine whether CeA^{GABA} neuronal activity contributes to post-stress breathing regulation, we recorded Ca^{2+} activity of CeA^{GABA} neurons after 30-min ARS. During the recording, animals freely explored in the WBP chamber while their breathing parameters, plethysmography traces and calcium activity were being recorded simultaneously. A 4-s window around the onset of increasing breathing rate was analyzed, with the period 4 s before breathing onset taken as baseline.

Optogenetic stimulation procedures

Three weeks after ChR2- or NpHR-encoding virus injections, mice were anesthetized with pentobarbital sodium (60 μg/g, i.p.). Before the surgical procedure, we carefully monitored the depth of anesthesia by assessing the mice's responses to the toe-pinch reflex. During the surgery, additional anesthetic was administered as needed (30% of the original dose, i.p.) to ensure that the mice remained immobile and pain-free throughout the operation. An optical fiber (OD, 200 μm; NA, 0.22) was unilaterally implanted into the CeA (AP, −0.8 mm; ML, ±2.65 mm; DV, −4.63 mm), LPBN (AP, −5.22 mm; ML, ±1.45 mm; DV, −3.50 mm), LC (AP, −5.51 mm; ML, ±0.85 mm; DV, −3.25 mm), NTS (AP, −7.30 mm; ML, ±0.5 mm; DV, −4.40 mm), preBötC (AP, −7.18 mm; ML, ±1.38 mm; DV, −5.85 mm), RTN (AP, −6.75 mm; ML, ±1.55 mm; DV, −5.93 mm) or PVT (AP, −0.80 ~ 1.20 mm; ML, 0 mm; DV, −3.05 mm) of the mice fixed in a stereotactic frame with a heating pad. Optogenetic stimulation was conducted via the delivery of blue (473 nm) or yellow (580 nm) light controlled by LED source stimulator (Newdoon Inc., China) one week after the fiber-implantation procedures to ensure adequate animal recovery. Photostimulation parameters were adjusted based on the experimental purpose. For in vivo photostimulation, the output power of light at the distal end of the optical fiber was consistently set to 8–10 mW, as measured using an optical power meter (PM20; Thorlabs, USA). In patch clamp recording experiments, the output power was adjusted to ~20 mW. Similar histological experiments were performed to validate ChR2 and NpHR expression, and electrophysiological recordings were conducted to further validate efficiency.

For resting breathing measurements, freely behaving mice were placed in WBP chamber and allowed to habituate for one hour before photostimulation. Then, the optical fiber was connected with patch cord of laser stimulator and given frequency-dependent (1 Hz, 5 Hz, 10 Hz, 20 Hz) tonic blue light (wavelength: 473 nm; width, 20 ms; power: 8–10 mW) stimulation for 1 min in behaviorally quiescent mice. Breathing parameters and plethysmography traces were recorded from 1 min before laser on to 1 min after the end of stimulation.

For behavioral tests, we connected the fiber implanted in mice to patch cord of laser stimulator and placed the mice into open field or plus maze. Then, the laser controller was turned on with blue light (wavelength: 473 nm; frequency: 10 Hz; width, 20 ms; power: 8–10 mW) and started to record the mice locomotion for 10 min.

For PND recordings, mice were anesthetized (urethane, 1.3 g/kg body weight, i.p.) and placed in a stereotaxic frame in a prone position. After occipital craniotomy, the skull was exposed and drilled above the CeA and LPBN, LC, NTS, and preBötC. Photostimulation of ChR2-transduced CeA^{GABA} neurons or terminals was accomplished by vertically placing the optical fiber (wavelength: 473 nm; frequency: 10 Hz; width, 20 ms; power: 8–10 mW; duration: 1 min) on the surface of the CeA and its terminals. The PND was recorded before and after photostimulation. NpHR-encoding CeA^{GABA} neurons were stimulated by continuous yellow light (wavelength: 580 nm; power: 8–10 mW; duration: 1 min) during PND recording.

Chemogenetics

The chemogenetic protocol was utilized as previously described[77,78]. For chemogenetic stimulation of CeA^{GABA} neurons, hM3Dq-mCherry virus vector was injected into CeA of Vgat-Cre mice. Four weeks after virus injections, we performed breathing measurement. To activate CeA^{GABA} neurons, mice were intraperitoneally administered with clozapine N-oxide (CNO; 1 mg/kg dissolved in 0.9% saline). Control mice were injected with the equal volume of saline (i.p.). To investigate the effects of activation of neurons on breathing physiologically, the measurement procedure was as follows: On the first day, mice were placed in chambers and allowed to explore novel environment for at least 6 h. On the second day, mice were allowed to adapt in chambers for 60 min and injected with saline during adaptation. At the same time of third day, mice were allowed to habituate in chambers for 60 min and received CNO injection. Breathing parameters were measured for 40 min and analyzed as mentioned above. Specific breathing patterns,

including sigh and apnea, were measured for 4 h. Histological experiments were performed at 4 weeks post-injection to validate hM3Dq-mCherry expression in the CeA, and electrophysiological recordings were conducted to verify the excitatory effect of hM3Dq.

To chemogenetically inhibit CeA^{GABA} neurons, the viral vector encoding hM4Di-eYFP was injected into CeA in Vgat-Cre mice. Breathing measurements were conducted four weeks post-injection. To investigate the effect of inhibition of CeA^{GABA} neurons in regulation of breathing patterns, the protocol was employed as described above in breathing measurement. To measure the response of behaviors in mice with anxiety-like behaviors, they were intraperitoneally administered with saline or CNO (2 mg/kg dissolved in 0.9% saline) and then placed back into their home cage. After the drug took effect after 30 min, mice were subjected to restraint stress for 30 min, then returned to their home cages for another 30-min freely behaving, followed by behavioral measurements. Statistical analysis, electrophysiological recordings, and histological experiments were conducted as described above.

Recording of PND

To assess the impact of CeA^{GABA} neurons on central drive to breathing, we performed PND recordings in anesthetized mice. Mice were anesthetized with urethane (1.3 g/kg body weight, i.p.), and supplementary doses of 0.1 g/kg were administered as needed. The protocol was employed as previously described[78]. Each mouse was placed in a stereotaxic frame in a prone position, and its body temperature was maintained at 37 °C using a program-controlled heating pad. They received a tracheostomy, and the vagus nerves were sectioned bilaterally. After administration of the paralyzing agent pancuronium (5 mg/kg body weight, i.p.), artificial ventilation with 100% O_2 was maintained throughout surgery in order to inactivate peripheral respiratory chemoreceptors. The left phrenic nerve was freed carefully from nearby tissues, placed on a silver bipolar electrode, and submerged in warm liquid paraffin. End-tidal CO_2 ($ETCO_2$), an indicator of the partial pressure of CO_2 in arterial blood, was continuously monitored with a capnograph (MicroCapStar, CWE Inc., USA) and maintained at approximately 4% as the basal level and modified as needed by altering the ventilation parameters. All analog data were processed through a micro1401 digitizer (Cambridge Electronic Design Ltd, UK) and analyzed off-line using Spike 2 software (Cambridge Electronic Design). The integrated PND was obtained by rectifying and smoothing (time constant, 0.1 s) the original signal, which was sampled at 2 kHz and filtered with a 30–3000 Hz bandpass. The frequency and peak amplitude of the integrated PND were measured for quantitative analysis.

Immunohistochemical staining

The animals were deeply anesthetized with urethane (1.8 g/kg, i.p.) and transcardially perfused with chilled saline, followed by paraformaldehyde (PFA, 4% in PBS, pH 7.4). After decapitation, the brains were removed and post-fixed for 24 h in 4% PFA at 4 °C, and subsequently transferred to a 30% PBS-buffered sucrose solution until it was saturated (24–36 h). Tissues were embedded in OCT compound, and stored at −80 °C before use. Coronal sections were cut at 25 µm on a freezing microtome (CM1950; Leica Microsystems, Germany). The sections were blocked in 5% bovine serum albumin (BSA) in PBS (0.25% Triton X-100 in PBS) for 30 min at room temperature (23–24 °C), followed by incubation with primary antibodies in 2% BSA-PBS overnight at 4 °C. Then the sections were washed with PBS (3 × 5 min) and incubated with fluorescent secondary antibodies at room temperature for 1 h. All rinses and incubations were done on a shaker at low speed. After rinsing with PBS (3 × 5 min), the sections were mounted on slides with Vectashield Antifade Mounting Medium (Vector Laboratories, Burlingame, CA, USA) for visualization. Images of whole-brain sections were captured using a laser-scanning confocal microscope (LSM 800, Carl Zeiss, Germany) and processed with ZEN software (Zeiss, Germany).

The primary antibodies used were as follows: chicken anti-GFP (dilution 1:2000, catalog# ab13970, RRID: AB_300798, Abcam), rabbit anti-NeuN (dilution 1:1000, Abcam, catalog# ab177487, RRID: AB_2532109), chicken anti-mCherry (dilution 1:2000, catalog# ab205402, RRID: AB_2725776, Abcam), mouse anti-Phox2b (dilution 1:500, catalog# sc-376997, Santa Cruz Biotechnology), mouse anti-TH (dilution 1:1000, EMD Millipore Corp, catalog# MAB318lu), rabbit anti-FoxP2 (dilution 1:1000, Abcam, catalog# ab16046, RRID: AB_1078909), rabbit anti-mCherry (dilution 1:1000, catalog# NBP2-25157, RRID: AB_2753204, Novus Biologicals). The fluorophore-conjugated secondary antibodies used were: Cy™3 AffiniPure goat anti-rabbit IgG (H + L) (dilution 1:500, Jackson ImmunoResearch Laboratories, catalog# 111-165-003, RRID: AB_2338000), goat polyclonal secondary antibody to chicken IgY-H&L (Alexa Fluor® 555) (dilution 1:1000, Abcam, catalog# ab150170, RRID: AB_2893330), goat polyclonal secondary antibody to chicken IgY-H&L (Alexa Fluor® 488) (dilution 1:1000, Abcam, catalog# ab150169, RRID: AB_2636803), goat polyclonal secondary antibody to mouse IgG-H&L (Alexa Fluor® 488) (dilution 1:1000, Abcam, catalog# ab150113, RRID: AB_2576208), AlexaFluor 488 AffiniPure alpaca anti-rabbit IgG (H + L) (dilution 1:500, catalog# 611-545-215, RRID: AB_2721874, Jackson ImmunoResearch Laboratories).

RNAscope Fluorescence in situ Hybridization

To detect the neural type of the CeA or LPBN, we prepared the tissue sections 4 weeks after virus injections and performed RNAscope-FISH as described before[81,82]. The mice were deeply anesthetized using urethane (1.8 g/kg, i.p.). Once the toe-pinch reflex disappeared, the mice underwent transcardial perfusion with chilled saline. Then, the mice were fixed with paraformaldehyde (PFA, 4%, 4 °C) and brain tissue was collected and immersed in PFA (4 °C) for 24 h. Subsequently, the tissue was dehydrated through a gradient of 15% and 30% sucrose phosphate buffer solution (PBS) and embedded in OCT and stored at −80 °C. Coronal sections at a thickness of 25 µm were obtained using a cryostat (CM1950, Leica Microsystems, Wetzlar, Germany). According to the manufacturer's user manual for the RNAscope® multichannel second-generation fluorescence kit (document no. 323100-USM), the slides were subjected to the RNAscope multiplex fluorescent assay. All RNAscope-FISH probes were designed and validated by Advanced Cell Diagnostics, Inc.

Subsequently, images were acquired via a confocal microscope (LSM 800; Carl Zeiss, Jena, Germany) and processed with the ZEN software program (Carl Zeiss). Cells were marked and categorized using the ImageJ cell counter plugin. Cells showing expression in the C1 channel for *mCherry* mRNA (Cat#431201, Advanced Cell Diagnostics, USA), C1 channel for *EGFP* mRNA (Cat#400281, Advanced Cell Diagnostics, USA), C1 channel for *eYFP* mRNA (Cat#312131, Advanced Cell Diagnostics, USA), C3 channel for *Slc17a6* mRNA (Cat#319171-C3, Advanced Cell Diagnostics, USA), C2 channel for *Slc32a1* mRNA (Cat#319191-C2, Advanced Cell Diagnostics, USA), C3 channel for *Slc32a1* mRNA (Cat#319191-C3, Advanced Cell Diagnostics, USA), C2 channel for *Gad2* mRNA (Cat#439371-C2, Advanced Cell Diagnostics, USA), C3 channel for *Slc17a7* mRNA (Cat#416631-C3, Advanced Cell Diagnostics, USA), were counted and marked. Expression was denoted in a binary yes/no format based on the fulfillment of defined criteria: the presence of at least five punctate fluorescent dots accompanying a nucleus labeled by DAPI Fluoromount-G (Cat#SBA-0100-20, SouthernBio, China). Cells identified as double-marked through this process were recognized as exhibiting colocalization.

Electrophysiological recording

Both cell-attached and whole-cell patch-clamp recordings were made in CeA^{GABA} neurons and $LPBN^{Glu}$ neurons projecting to the preBötC.

Four weeks after virus injection, transverse brain slices were prepared after rapid decapitation under anesthesia (5% pentobarbital sodium, 1.5 mL/kg, i.p.). As previously reported[83,84], coronal slices (250 μm) were cut on a vibrating microtome (VT1200S, Leica Biosystems, Germany) in ice-cold sucrose-containing solution (in mM: 260 sucrose, 3 KCl, 5 $MgCl_2$, 1 $CaCl_2$, 1.25 NaH_2PO_4, 26 $NaHCO_3$, 10 glucose, and 1 kynurenic acid). Slices were incubated for 30 min to 1 h at 33 °C and subsequently at room temperature in aCSF (in mM: 118 NaCl, 6 KCl, 1.25 NaH_2PO_4, 25 $NaHCO_3$, 2 $CaCl_2$, 1 $MgCl_2$, and 25 glucose). All cutting and incubation solutions were bubbled with 95% O_2 and 5% CO_2. We chose fluorescence-tagged target neurons for patch-clamp slice recordings in a perfusion chamber on fixed-stage fluorescence microscopes equipped with infrared Nomarski optics (Carl Zeiss AxioExaminer and Olympus Optical BX51WI). Slices were perfused at ~31 °C with oxygenated aCSF at a speed of 2 mL/min. Signals were amplified with a Multiclamp 700B amplifier (Molecular Devices), filtered at 1 KHz (Bessel low-pass), and sampled at 10 kHz (Digidata 1440 A, Molecular Devices). Recording electrodes (4–6 MΩ) were filled with a solution containing the following components (in mmol/L): 10 NaCl, 130 K^+ gluconate, 11 EGTA, 1 $CaCl_2$, 10 HEPES, 1 $MgCl_2$, 2 MgATP, and 0.2 NaGTP, pH 7.3 (295 - 300 mOsm).

Specifically, photostimulation (wavelength: 473 nm; 20-ms pulse width; frequency: 10 Hz; power: 20 mW, duration: 10 sec) of ChR2-expressing axonal terminals of CeA^{GABA} neurons projecting to the LPBN was employed to regulate the activity of $LPBN^{Glu}$ neurons projecting to the preBötC. Spontaneous firing was recorded in $LPBN^{Glu}$ neurons projecting to the preBötC using a cell-attached mode at a holding potential of −60 mV, while resting membrane potential and action potential discharge were recorded in a whole-cell current clamp mode. Firing rate histograms were generated by integrating action potential discharge in a 10-s bin using Spike2 software (Cambridge Electronic Design). We further examined whether $LPBN^{Glu}$ neurons projecting to the preBötC received inhibitory monosynaptic inputs from CeA^{GABA} neurons. Whole-cell patch clamp recordings were performed to monitor light-evoked IPSC. Drugs were applied at the following concentrations: TTX, 1 μM; 4-AP, 100 μM; PTX, 50 μM.

Statistical analysis

All experiments and data analyses were conducted in a blinded manner, encompassing WBP and behavioral tests, immunohistochemistry, and electrophysiological recordings. Data were analyzed using GraphPad Prism (V9.4.0), Smart (V3.0), ZEN (V3.4), Spike2 (V8.0), Clampfit (V10.6), ImageJ (V1.54 g), MATLAB (R2017a), IOX 2.10, and FinePointe. Representative micrographs presented in the manuscript were derived from experiments repeated in at least three mice, each with multiple brain slices, yielding consistent results.

For two-group unpaired comparisons involving a single factor, data with a normal distribution were analyzed using a two-tailed unpaired *t*-test, while data that did not follow a normal distribution were analyzed using a two-tailed Mann–Whitney *U*-test. In cases where the data exhibited a normal distribution but had heterogeneous variances, a two-tailed unpaired t-test with Welch's correction was employed. For two-group paired comparisons involving a single factor, data with a normal distribution were analyzed using a two-tailed paired *t*-test, and data without a normal distribution were analyzed using a two-tailed Wilcoxon matched-pairs signed-rank test.

For unpaired comparisons involving three or more groups and a single factor, data with a normal distribution were analyzed using ordinary one-way ANOVA, followed by post-hoc multiple comparisons tests such as Dunnett, Tukey, or Bonferroni. Data that did not follow a normal distribution were analyzed using either the Brown-Forsythe and Welch ANOVA tests with Šídák's multiple comparisons test or the Kruskal-Wallis test with post-hoc Dunn's multiple comparisons test. For paired comparisons involving three or more groups and a single factor, data with a normal distribution were analyzed using repeated measures one-way ANOVA, followed by post-hoc Tukey's multiple comparisons test. Data without a normal distribution were analyzed using the two-sided Friedman test, followed by post-hoc Dunn's multiple comparisons test.

Comparisons between groups with two factors were analyzed using two-way ANOVA, with Bonferroni's, Šídák's, or Tukey's multiple comparisons test. Two-way ANOVA followed by uncorrected Fisher's LSD was also used for two groups comparison with two factors. Pearson correlation coefficients were used for a correlation analysis.

Statistical details, including animal numbers, p values, and statistical test types, are described in the figure legends or Supplementary Table 1. The data are presented as means ± SEM, with statistical significance defined as $^{*}p < 0.05$, $^{**}p < 0.01$, $^{***}p < 0.001$ and $^{****}p < 0.0001$.

Reporting summary

Further information on research design is available in the Nature Portfolio Reporting Summary linked to this article.

Data availability

Source data are provided with this paper. All data are contained in the main text and the supplementary materials. Source data are provided with this paper.

References

1. Yang, C. F., Kim, E. J., Callaway, E. M. & Feldman, J. L. Monosynaptic projections to excitatory and inhibitory preBotzinger complex neurons. *Front. Neuroanat.* **14**, 58 (2020).
2. Boiten, F. A., Frijda, N. H. & Wientjes, C. J. Emotions and respiratory patterns: review and critical analysis. *Int. J. Psychophysiol.* **17**, 103–128 (1994).
3. Del Negro, C. A., Funk, G. D. & Feldman, J. L. Breathing matters. *Nat. Rev. Neurosci.* **19**, 351–367 (2018).
4. Feldman, J. L., Del Negro, C. A. & Gray, P. A. Understanding the rhythm of breathing: so near, yet so far. *Annu. Rev. Physiol.* **75**, 423–452 (2013).
5. Smith, J. C., Abdala, A. P., Rybak, I. A. & Paton, J. F. Structural and functional architecture of respiratory networks in the mammalian brainstem. *Philos. Trans. R. Soc. Lond. B Biol. Sci.* **364**, 2577–2587 (2009).
6. Tipton, M. J., Harper, A., Paton, J. F. R. & Costello, J. T. The human ventilatory response to stress: rate or depth? *J. Physiol.* **595**, 5729–5752 (2017).
7. Masaoka, Y. & Homma, I. The effect of anticipatory anxiety on breathing and metabolism in humans. *Respir. Physiol.* **128**, 171–177 (2001).
8. Jerath, R. & Beveridge, C. Respiratory rhythm, autonomic modulation, and the spectrum of emotions: the future of emotion recognition and modulation. *Front. Psychol.* **11**, 1980 (2020).
9. Homma, I. & Masaoka, Y. Breathing rhythms and emotions. *Exp. Physiol.* **93**, 1011–1021 (2008).
10. Boiten, F. A. The effects of emotional behaviour on components of the respiratory cycle. *Biol. Psychol.* **49**, 29–51 (1998).
11. Craske, M. G. & Stein, M. B. Anxiety. *Lancet* **388**, 3048–3059 (2016).
12. Weng, H. Y. et al. Interventions and manipulations of interoception. *Trends Neurosci.* **44**, 52–62 (2021).
13. Abelson, J. L., Weg, J. G., Nesse, R. M. & Curtis, G. C. Persistent respiratory irregularity in patients with panic disorder. *Biol. Psychiatry* **49**, 588–595 (2001).
14. Stein, M. B., Millar, T. W., Larsen, D. K. & Kryger, M. H. Irregular breathing during sleep in patients with panic disorder. *Am. J. Psychiatry* **152**, 1168–1173 (1995).
15. Yackle, K. et al. Breathing control center neurons that promote arousal in mice. *Science* **355**, 1411–1415 (2017).
16. Onimaru, H. & Homma, I. Spontaneous oscillatory burst activity in the piriform-amygdala region and its relation to in vitro respiratory activity in newborn rats. *Neuroscience* **144**, 387–394 (2007).

17. Sah, P., Faber, E. S., Lopez De Armentia, M. & Power, J. The amygdaloid complex: anatomy and physiology. *Physiol. Rev.* **83**, 803–834 (2003).
18. Adolphs, R., Tranel, D., Damasio, H. & Damasio, A. R. Fear and the human amygdala. *J. Neurosci.* **15**, 5879–5891 (1995).
19. Pitkanen, A. & Amaral, D. G. The distribution of GABAergic cells, fibers, and terminals in the monkey amygdaloid complex: an immunohistochemical and in situ hybridization study. *J. Neurosci.* **14**, 2200–2224 (1994).
20. Roberto, M., Kirson, D., Khom, S. The role of the central amygdala in alcohol dependence. *Cold Spring Harb Perspect Med.* **11**, a039339 (2021).
21. Tye, K. M. et al. Amygdala circuitry mediating reversible and bidirectional control of anxiety. *Nature* **471**, 358–362 (2011).
22. Duvarci, S. & Pare, D. Amygdala microcircuits controlling learned fear. *Neuron* **82**, 966–980 (2014).
23. Borkar, C. D. et al. Top-down control of flight by a non-canonical cortico-amygdala pathway. *Nature* **625**, 743–749 (2024).
24. Wang, Q. et al. Insular cortical circuits as an executive gateway to decipher threat or extinction memory via distinct subcortical pathways. *Nat. Commun.* **13**, 5540 (2022).
25. Ressler, R. L. & Maren, S. Synaptic encoding of fear memories in the amygdala. *Curr. Opin. Neurobiol.* **54**, 54–59 (2019).
26. Babaev, O., Piletti Chatain, C. & Krueger-Burg, D. Inhibition in the amygdala anxiety circuitry. *Exp. Mol. Med.* **50**, 1–16 (2018).
27. Liu, W. Z. et al. Identification of a prefrontal cortex-to-amygdala pathway for chronic stress-induced anxiety. *Nat. Commun.* **11**, 2221 (2020).
28. Zhang, X. et al. Brain control of humoral immune responses amenable to behavioural modulation. *Nature* **581**, 204–208 (2020).
29. Hsu, D. T., Chen, F. L., Takahashi, L. K. & Kalin, N. H. Rapid stress-induced elevations in corticotropin-releasing hormone mRNA in rat central amygdala nucleus and hypothalamic paraventricular nucleus: an in situ hybridization analysis. *Brain Res.* **788**, 305–310 (1998).
30. Zhao, J. et al. A paraventricular thalamus to central amygdala neural circuit modulates acute stress-induced heightened wakefulness. *Cell Rep.* **41**, 111824 (2022).
31. Ma, J. et al. Divergent projections of the paraventricular nucleus of the thalamus mediate the selection of passive and active defensive behaviors. *Nat. Neurosci.* **24**, 1429–1440 (2021).
32. Rodriguez-Sierra, O. E., Goswami, S., Turesson, H. K. & Pare, D. Altered responsiveness of BNST and amygdala neurons in trauma-induced anxiety. *Transl. Psychiatry* **6**, e857 (2016).
33. Pedersen, W. S. et al. Higher resting-state BNST-CeA connectivity is associated with greater corrugator supercilii reactivity to negatively valenced images. *NeuroImage* **207**, 116428 (2020).
34. Wang, Y. et al. Multimodal mapping of cell types and projections in the central nucleus of the amygdala. *Elife* **12**, e84262 (2023).
35. Huang, D., Grady, F. S., Peltekian, L. & Geerling, J. C. Efferent projections of Vglut2, Foxp2, and Pdyn parabrachial neurons in mice. *J. Comp. Neurol.* **529**, 657–693 (2021).
36. Zimprich, A. et al. A robust and reliable non-invasive test for stress responsivity in mice. *Front. Behav. Neurosci.* **8**, 125 (2014).
37. Janak, P. H. & Tye, K. M. From circuits to behaviour in the amygdala. *Nature* **517**, 284–292 (2015).
38. Gilpin, N. W., Herman, M. A. & Roberto, M. The central amygdala as an integrative hub for anxiety and alcohol use disorders. *Biol. Psychiatry* **77**, 859–869 (2015).
39. Sah, P. Fear, anxiety, and the amygdala. *Neuron* **96**, 1–2 (2017).
40. Baas, D., Aleman, A. & Kahn, R. S. Lateralization of amygdala activation: a systematic review of functional neuroimaging studies. *Brain Res. Brain Res, Rev.* **45**, 96–103 (2004).
41. Sadler, K. E. et al. Divergent functions of the left and right central amygdala in visceral nociception. *Pain* **158**, 747–759 (2017).
42. Vlemincx, E., Van Diest, I. & Van den Bergh, O. Emotion, sighing, and respiratory variability. *Psychophysiology* **52**, 657–666 (2015).
43. Casarrubea, M. et al. Effects of chronic nicotine on the temporal structure of anxiety-related behavior in rats tested in hole-board. *Prog. Neuropsychopharmacol. Biol. Psychiatry* **96**, 109731 (2020).
44. O'Leary, T. P. et al. Neuronal cell types, projections, and spatial organization of the central amygdala. *iScience* **25**, 105497 (2022).
45. Tsai, N. Y. et al. Trans-Seq maps a selective mammalian retinotectal synapse instructed by Nephronectin. *Nat. Neurosci.* **25**, 659–674 (2022).
46. Cui, Y. et al. Defining preBotzinger complex rhythm- and pattern-generating neural microcircuits in vivo. *Neuron* **91**, 602–614 (2016).
47. Liu, N. et al. Respiratory control by Phox2b-expressing neurons in a locus coeruleus-prebotzinger complex circuit. *Neurosci. Bull.* **37**, 31–44 (2021).
48. Yang, C. F. & Feldman, J. L. Efferent projections of excitatory and inhibitory preBotzinger Complex neurons. *J. Comp. Neurol.* **526**, 1389–1402 (2018).
49. Arthurs, J. W., Bowen, A. J., Palmiter, R. D. & Baertsch, N. A. Parabrachial tachykinin1-expressing neurons involved in state-dependent breathing control. *Nat. Commun.* **14**, 963 (2023).
50. Yang, C. F. et al. Sexually dimorphic neurons in the ventromedial hypothalamus govern mating in both sexes and aggression in males. *Cell* **153**, 896–909 (2013).
51. Zhao, D. et al. The paraventricular thalamus input to central amygdala controls depression-related behaviors. *Exp. Neurol.* **342**, 113744 (2021).
52. Liang, S. H. et al. A neural circuit from thalamic paraventricular nucleus to central amygdala for the facilitation of neuropathic pain. *J. Neurosci.* **40**, 7837–7854 (2020).
53. Homma, I. & Phillips, A. G. Critical roles for breathing in the genesis and modulation of emotional states. *Handb. Clin. Neurol.* **188**, 151–178 (2022).
54. Harrison, O. K. et al. Interoception of breathing and its relationship with anxiety. *Neuron* **109**, 4080–4093 e4088 (2021).
55. Freire, R. C. & Nardi, A. E. Panic disorder and the respiratory system: clinical subtype and challenge tests. *Braz. J. Psychiatry* **34**, S32–S41 (2012).
56. Masaoka, Y. & Homma, I. Anxiety and respiratory patterns: their relationship during mental stress and physical load. *Int J. Psychophysiol.* **27**, 153–159 (1997).
57. Masaoka, Y., Sugiyama, H., Katayama, A., Kashiwagi, M. & Homma, I. Remembering the past with slow breathing associated with activity in the parahippocampus and amygdala. *Neurosci. Lett.* **521**, 98–103 (2012).
58. Sun, J. et al. Excitatory SST neurons in the medial paralemniscal nucleus control repetitive self-grooming and encode reward. *Neuron* **110**, 3356–3373.e3358 (2022).
59. Chen, D. et al. Microglia govern the extinction of acute stress-induced anxiety-like behaviors in male mice. *Nat. Commun.* **15**, 449 (2024).
60. Kalueff, A. V. et al. Neurobiology of rodent self-grooming and its value for translational neuroscience. *Nat. Rev. Neurosci.* **17**, 45–59 (2016).
61. Kalueff, A. V., Aldridge, J. W., LaPorte, J. L., Murphy, D. L. & Tuohimaa, P. Analyzing grooming microstructure in neurobehavioral experiments. *Nat. Protoc.* **2**, 2538–2544 (2007).
62. Kalueff, A. V. & Tuohimaa, P. Mouse grooming microstructure is a reliable anxiety marker bidirectionally sensitive to GABAergic drugs. *Eur. J. Pharmacol.* **508**, 147–153 (2005).
63. Zhang, Y. F. et al. Ventral striatal islands of Calleja neurons bidirectionally mediate depression-like behaviors in mice. *Nat. Commun.* **14**, 6887 (2023).
64. Klenowski, P. M. et al. A neuronal coping mechanism linking stress-induced anxiety to motivation for reward. *Sci. Adv.* **9**, eadh9620 (2023).

65. Nagarajan, N. & Capecchi, M. R. Optogenetic stimulation of mouse Hoxb8 microglia in specific regions of the brain induces anxiety, grooming, or both. *Mol. Psychiatry* **29**, 1726–1740 (2024).
66. Wang, B. et al. Zfp462 deficiency causes anxiety-like behaviors with excessive self-grooming in mice. *Genes Brain Behav.* **16**, 296–307 (2017).
67. Wachowiak, M. All in a sniff: olfaction as a model for active sensing. *Neuron* **71**, 962–973 (2011).
68. He, W. et al. Activation of glutamatergic neurons in the organum vasculosum of the lamina terminalis induces thirst-driven sniffing. *Cell Rep.* **44**, 115254 (2025).
69. Casarrubea, M., Di Giovanni, G., Aiello, S. & Crescimanno, G. The hole-board apparatus in the study of anxiety. *Physiol. Behav.* **271**, 114346 (2023).
70. Johnson, E. O., Roth, T. & Breslau, N. The association of insomnia with anxiety disorders and depression: exploration of the direction of risk. *J. Psychiatr. Res.* **40**, 700–708 (2006).
71. Hong, W., Kim, D. W. & Anderson, D. J. Antagonistic control of social versus repetitive self-grooming behaviors by separable amygdala neuronal subsets. *Cell* **158**, 1348–1361 (2014).
72. Lacuey, N., Hampson, J. P., Harper, R. M., Miller, J. P. & Lhatoo, S. Limbic and paralimbic structures driving ictal central apnea. *Neurology* **92**, e655–e669 (2019).
73. Tahmasian, M. et al. Structural and functional neural adaptations in obstructive sleep apnea: an activation likelihood estimation meta-analysis. *Neurosci. Biobehav. Rev.* **65**, 142–156 (2016).
74. Liu, J. et al. Differential efferent projections of GABAergic neurons in the basolateral and central nucleus of amygdala in mice. *Neurosci. Lett.* **745**, 135621 (2021).
75. Gallo, G. The cytoskeletal and signaling mechanisms of axon collateral branching. *Dev. Neurobiol.* **71**, 201–220 (2011).
76. Liu, S. et al. Divergent brainstem opioidergic pathways that coordinate breathing with pain and emotions. *Neuron* **110**, 857–873 e859 (2022).
77. Fu, C. et al. Activation of Phox2b-expressing neurons in the nucleus tractus solitarii drives breathing in mice. *J. Neurosci.* **39**, 2837–2846 (2019).
78. Yu, H. et al. A neural circuit mechanism controlling breathing by leptin in the nucleus tractus solitarii. *Neurosci. Bull.* **38**, 149–165 (2022).
79. Jun, S. et al. Circuit-specific control of blood pressure by PNMT-expressing nucleus tractus solitarii neurons. *Neurosci. Bull.* **39**, 1193–1209 (2023).
80. Paxinos, G. & Franklin, K. B. J. *The mouse brain in Stereotaxic Coordinates*, 2nd edn. (Academic Press, 2003).
81. Wang, Y. et al. Control of breathing by orexinergic signaling in the nucleus tractus solitarii. *Sci. Rep.* **14**, 7473 (2024).
82. Zhu, M. et al. Mapping of afferent and efferent connections of phenylethanolamine N-methyltransferase-expressing neurons in the nucleus tractus solitarii. *CNS Neurosci. Ther.* **30**, e14808 (2024).
83. Wang, S., Shi, Y., Shu, S., Guyenet, P. G. & Bayliss, D. A. Phox2b-expressing retrotrapezoid neurons are intrinsically responsive to H^+ and CO^2. *J. Neurosci.* **33**, 7756–7761 (2013).
84. Wang, S. et al. TASK-2 channels contribute to pH sensitivity of retrotrapezoid nucleus chemoreceptor neurons. *J. Neurosci.* **33**, 16033–16044 (2013).

Acknowledgements

This work was supported by grants from the Natural Science Foundation of China (3217090344, U23A20431, S.W.), Hebei Province Yanzhao Golden Platform Project (HJZD202510, F.Y.), Natural Science Foundation of Hebei Province for Innovative Research Group Project (H2021206203, S.W.) and Postdoctoral Science Foundation of Hebei Medical University (HB202506, X.W.). We thank the Core Facilities and Centers, Institute of Medicine and Health, Hebei Medical University for technical support.

Author contributions

X.W. and S.B. designed the experiments, analyzed the data, and wrote the manuscript. Z.Y. and Y.L. performed breathing measurements and analyzed the WBP results. X.C. and L. Shao performed behavior tests; H.Y. and X.J. performed viral injections and optical fiber implantation. L. Shi and T.D. performed ex vivo electrophysiological recording. C.W. and W.H. analyzed immunohistochemical data. Y.W. performed recording of phrenic nerve discharge. S.W. and F.Y. were responsible for study concept and design. S.W. and F.Y. drafted the article. S.W. obtained research funding. All authors approved the version to be published.

Competing interests

The authors declare no competing interests.

Additional information

Supplementary information The online version contains supplementary material available at https://doi.org/10.1038/s41467-025-58791-6.

Correspondence and requests for materials should be addressed to Fang Yuan or Sheng Wang.

Peer review information *Nature Communications* thanks Chen Li, Michael Fanselow and the other, anonymous, reviewer(s) for their contribution to the peer review of this work. A peer review file is available.